

A THEORETICAL APPROACH TOWARDS THE MODELING OF  
VIBROTHERMOGRAPHY USING FINITE ELEMENT METHODS

by

Vibhor Bhargava

A Thesis presented to the Faculty of the  
American University of Sharjah  
College of Engineering  
In Partial Fulfilment  
of the Requirements  
for the Degree of

Master of Science in  
Mechanical Engineering

Sharjah, United Arab Emirates

April 2019



## Approval Signatures

We, the undersigned, approve the master's Thesis of Vibhor Bhargava

Thesis Title: A Theoretical Approach Towards the Modeling of Vibrothermography Using Finite Element Methods

**Signature**

**Date of Signature**

(dd/mm/yyyy)

---

Dr. Bassam Abu-Nabah

Assistant Professor, Department of Mechanical Engineering  
Thesis Advisor

---

Dr. Maen Alkhader

Associate Professor, Department of Mechanical Engineering  
Thesis Co-Advisor

---

Dr. Mohammad Hamdan

Associate Professor, Department of Mechanical Engineering  
Thesis Committee Member

---

Dr. Mahmoud Awad

Associate Professor, Department of Industrial Engineering  
Thesis Committee Member

---

Dr. Mamoun Abdel-Hafez

Head, Department of Mechanical Engineering

---

Dr. Lotfi Romdhane

Associate Dean for Graduate Affairs and Research  
College of Engineering

---

Dr. Naif Darwish

Acting Dean, College of Engineering

---

Dr. Mohamed El-Tarhuni

Vice Provost for Graduate Studies

## **Acknowledgement**

I would like to thank my advisors, Dr. Bassam Abu-Nabah and Dr. Maen Alkhader, for their guidance and advice throughout this thesis. I am extremely thankful for their support and assistance that kept me motivated throughout my research.

I would also like to thank the Department of Mechanical Engineering at the American University of Sharjah for offering me a teaching assistantship all through my postgraduate program.

Finally, I would like to thank my family for their encouragement and support.

## Abstract

The demand for preventive maintenance in the aerospace industry has been growing as part of life extension programs. Due to its reduced inspection time, part preparation requirements, floor space, and environmental concerns, vibrothermography has become an attractive solution to these programs as a potential replacement to conventional surface inspection methods. It offers the capability to detect surface cracks mainly through capturing vibration-induced frictional heat generation of contacting crack surfaces. The multidisciplinary nature of this inspection technology makes it rather difficult to theoretically capture the system response without the proper application of finite element (FE) methods. It requires relating the material mechanical and thermal properties in a coupled finite element model to properly address wave propagation, contact mechanics, fracture mechanics, friction heat generation and heat diffusion in simulated inspections. In this study, a theoretical model is developed to estimate the dynamic strain response at any location in commonly used cantilever beams oscillating at a given frequency. This model is utilized to assess the convergence of FE-based dynamic system response while determining the element size requirements to realistically model elastic wave propagation throughout the sample. Three different meshing criteria are assessed to properly capture the singularity at the crack tip. It is demonstrated that the use of solid element circular meshing criteria converges to singular quarter-node solid element solution and allows coupling it with heat generation and diffusion around the vicinity of a crack to deliver the most effective approach for modelling vibrothermography. Any deviation from the optimized meshing criteria and element size requirements will adversely affect the relative motion of crack surfaces and frictional heat generation. This effort brings FE modeling of vibrothermography a step closer towards realistic inspection simulation in the future.

**Keywords:** *Sonic Infrared, Vibrothermography, Crack, Heating Index, Finite Element Method, Meshing*

## Table of Contents

Abstract .....	5
List of Figures .....	8
List of Tables .....	10
List of Abbreviations .....	11
Chapter 1. Introduction .....	12
1.1. Overview .....	12
1.2. Thesis Objectives .....	13
1.3. Research Contribution .....	14
1.4. Thesis Organization .....	15
Chapter 2. Background and Literature Review.....	16
2.1. Types of Heating.....	16
2.1.1. Frictional heating.....	16
2.1.2. Viscoelastic heating.....	16
2.1.3. Plastic heating.....	18
2.2. Parameters Affecting Heat Generation .....	19
2.2.1. Crack motion .....	19
2.2.2. Crack length.....	19
2.2.3. Vibration power.....	20
2.2.4. Acoustic chaos.....	20
2.2.5. Crack closure .....	21
2.2.6. Material properties.....	22
2.3. System Setup.....	22
Chapter 3. Finite Element Modeling of Vibrothermography.....	24
3.1. Stress Intensity Factor .....	25
3.2. Proposed Model Design.....	29
3.3. Damping.....	29
3.3.1. Effect of damping on stable time increment.....	31
3.4. Friction.....	32
3.4.1. Friction coefficient .....	33
3.5. Explicit Dynamic Analysis .....	34
3.6. Stability .....	35
3.6.1. Stable time increment.....	36
3.6.2. Dilatational wave speed.....	36

3.7.	Contact .....	37
3.7.1.	Surface properties .....	37
3.8.	Meshing.....	38
3.9.	Load, Boundary and Initial Conditions.....	40
Chapter 4.	Theoretical Solution .....	43
Chapter 5.	Modal and Harmonic Response Results.....	47
5.1.	Fast Fourier Transform .....	47
5.1.1.	Short time Fourier transform .....	47
5.1.2.	STFT time dependency.....	49
5.2.	Modal and Harmonic Response Analysis .....	50
5.2.1.	Mechanical vibrations .....	50
5.2.2.	Modal analysis.....	51
5.2.3.	Explicit harmonic response .....	52
Chapter 6.	Heat Generation Results.....	54
6.1.	Heat Generation Analysis .....	54
6.2.	Temperature Maps .....	57
6.3.	Hybrid Case .....	60
6.4.	Validating the Model .....	61
6.5.	Heating Index.....	64
Chapter 7.	Conclusion and Future Work .....	69
References	.....	71
Vita	.....	73

## List of Figures

Figure 2.1: Stress-strain curve showing the difference between (a) viscoelastic material and (b) purely elastic material.....	17
Figure 2.2: Three principal modes of vibration showing crack face motion (a) tensile mode (clapping), (b) in-plane shear mode (rubbing) and (c) anti-plane shear mode (tearing).....	19
Figure 2.3: Schematic representation of a sonic IR system .....	23
Figure 3.1: Schematic representation of the model used for estimating SIF ( $K_I$ ) at the crack tip .....	27
Figure 3.2: Schematic of the quarter node wedge shape elements around a crack tip.....	27
Figure 3.3: Meshed model created in ABAQUS with quarter node wedge shape elements at the crack tip .....	27
Figure 3.4: Close up view of the crack tip showing the circular fan mesh.....	27
Figure 3.5: The effect of selecting the element type and meshing criteria in estimating the SIF ( $K_I$ ).....	28
Figure 3.6: The proposed design model meshed using (a) rectangular mesh, (b) semi-circular mesh and (c) circular mesh .....	39
Figure 3.7: Close up view of the mesh around the crack.....	39
Figure 3.8: Load and boundary conditions applied on the model under analysis.....	41
Figure 4.1: Schematic representation of the theoretical model.....	43
Figure 4.2: Theoretical solution obtained upon solving Equation (28) at $x = 150$ mm .....	45
Figure 4.3: Surface strain along the bar using different frequencies .....	46
Figure 4.4: Surface strain along the bar using the combination of all frequencies.....	46
Figure 5.1: Finite element simulation of strain variation over the excitation period at $x = 150$ mm and $y = 7.5$ mm using a coarse mesh .....	48
Figure 5.2: Spectrum of frequencies obtained upon performing STFT .....	48
Figure 5.3: FFT taken from the spectrum at a single time value .....	49
Figure 5.4: Frequency vs amplitude plot depicting the effect time has on the STFT.....	49
Figure 5.5: Model created in ABAQUS for performing the modal analysis .....	51
Figure 5.6: Assumed strain gauge position at the bottom of the bar .....	52
Figure 5.7: Frequency vs amplitude plot comparing the harmonic response for various mesh sizes.....	53
Figure 6.1: Shows the nodes considered for calculating the average temperature over the crack .....	54
Figure 6.2: Temperature variation with time using different mesh criteria for the 5 mm crack.....	55
Figure 6.3: Time vs temperature plots: (a) 2 mm, (b) 3 mm, (c) 4 mm, (d) 5 mm and (e) 6 mm cracks simulated using circular mesh criteria.....	56
Figure 6.4: Temperature maps for the 5 mm crack using different coarse mesh types at 0.7 s .....	57
Figure 6.5: Temperature maps for the 5 mm crack using different normal mesh types at 0.7 s .....	58
Figure 6.6: Temperature maps for the 5 mm crack using different fine mesh types at 0.7 s .....	59



Figure 6.7: A case of hybrid mesh in which the bar transitions from a coarse to a fine mesh in the middle around the crack .....	60
Figure 6.8: Time vs temperature plot exhibiting the effect of different criteria of circular meshes.....	60
Figure 6.9: Temperature maps for 5 mm crack using hybrid mesh at 0.7 s: (a) top view and (b) side view .....	61
Figure 6.10: Bar containing a 1.4 mm crack, used for validating the models designed in ABAQUS .....	62
Figure 6.11: Load and boundary conditions applied on the bar depicted in Figure (6.10), part (a) overview of the bar with the applied boundary conditions, part (b) the fixed left side end and part (c) the displacement load applied on the top right surface.....	63
Figure 6.12: Temperature map as seen from the top, for the model shown in Figure (6.10 and 6.11) .....	64
Figure 6.13: Temperature map as seen from the side, for the model shown in Figure (6.10 and 6.11) .....	64
Figure 6.14: Time vs temperature plot for the model illustrated in Figure (6.10).....	65
Figure 6.15: An example showing the process of calculation of heating index, (a) the strain output from ABAQUS, (b) energy index vs time and (c) heating index vs time .....	67
Figure 6.16: Time vs heating index plot for a 5 mm crack comparing different types of fine mesh .....	68
Figure 6.17: Time vs heating index plot for circular fine mesh comparing different crack sizes .....	68

## List of Tables

Table 3.1: Medium carbon steel material properties used in ABAQUS.....	29
Table 3.2: Mechanical damping properties.....	34
Table 3.3: Surface properties: thermal conductance parameters .....	38
Table 3.4: Mesh classification showing cross-sectional view of meshes with different element sizes.....	40
Table 5.1: Modal frequencies for the model illustrated in Figure (5.5).....	51
Table 5.2: Number of strain gauge elements for different meshes .....	52

## **List of Abbreviations**

FE	Finite Element
FEA	Finite Element Analysis
FEM	Finite Element Method
FFT	Fast Fourier Transform
IR	Infrared
MTS	Maximum Tangential Stress
MERR	Maximum Energy Release Rate
SIF	Stress Intensity Factor
STFT	Short Time Fourier Transform

## Chapter 1. Introduction

### 1.1. Overview

Vibrothermography, also known as sonic infrared (IR), is a nondestructive evaluation technique that is used for the detection of surface and subsurface cracks. The damaged part is vibrated using a sonic transducer, which results in heat generation around the crack tip and crack surface. IR cameras are used to detect the thermal variations in the specimen being inspected. Henekke et al. [1] were the first to introduce the method of vibrothermography in 1980. The work was based on detecting defects in composite materials, where heat is generated the most when resonance vibrations are achieved. Due to the limited technology at the time, the technique was not followed upon. The advent of advanced IR cameras put vibrothermography back into picture as a potential tool for crack detection.

This technique proved to be more advantageous in crack detection compared to other conventional methods, as it can inspect wider areas. Vibrothermography analysis generally involves three stages, namely vibration, crack heat generation and heat detection from the specimen. These three stages are equally important for crack detectability and size estimation.

The sample is vibrated using a sonic transducer. This vibration energy is converted into heat at the crack location. Though vibrothermography can cover large areas during the analysis process, it still requires several trials before one can be sure that all the cracks have been detected in the specimen. This is because the vibration modes are dependent on the sample geometry and material properties. Due to the incurred vibration, the area or part under observation generates significant amount of heat. Heat generated in the inspected parts is commonly attributed to frictional, viscoelastic and plastic heat generation. Heat detection is equally important for crack detection in a vibrothermographic analysis. A poor heat detection system may result in not detecting the crack at all. An IR camera is used for detecting cracks during a vibrothermographic analysis. The selected IR camera must take into account the material thermal properties to obtain a reliable result. Thermal properties, such as surface emissivity and thermal diffusivity, are essential to enhance crack detection capabilities. If the material has low surface emissivity, it will make crack detection

difficult. Additionally, high thermal conductivity will make the heat diffuse away too quickly, which will again make crack detection difficult. Another important factor that affects heat detection is the location of the crack. A surface crack is easily detected since it directly radiates heat to the IR camera. However, a subsurface crack, if the crack is located too deep, might not be detected by the IR camera.

Vibrothermography is a fast-establishing technique and a promising tool in the detection of cracks in aerospace components. But still, it is not practically accepted in industries due to the problem of repeatability. Ongoing research in this field is primarily focused on developing vibrothermography as a reliable technique in accordance with industrial standards. This thesis aims to attain a better understanding of the process of vibrothermography. Doing this should help in overcoming the problem of repeatability and progress vibrothermography, a step further towards being accepted as an industrial tool for crack detection.

## **1.2. Thesis Objectives**

Though vibrothermography is a fast and reliable technique, still it is not used commercially due to its shortcomings. The main problem concerning a vibrothermographic analysis is its repeatability. When the sample undergoes excitation, after a certain time due to tribological defects, the heat generation is attenuated. Work done by Renshaw et al. [2] explores the problem of repeatability of the vibrothermography technique. The crack surfaces upon vibration rub against each other, which might result in plastic deformation and cause the problem of repeatability. The crack surfaces might undergo plastic deformation, fretting, adhesive wear, oxidation and melting. It was observed that when the specimen was vibrated about 1000 times, a significant decrease in temperature was recorded. It was also concluded that, if the specimen was induced with stresses less than 30% of the endurance limit, no tribological defects such as plastic deformation, fretting, etc. were observed. Further increase in stress resulted in different tribological defects at different steps.

Holland et al. [3] also worked to overcome this obstacle by running several tests at three different sites with different experimental setups. The loading conditions were kept identical for all the experiments; all the specimens were vibrated under similar conditions of mode and power. It was concluded that all the experiments give

similar results for detectability of a crack in a specimen. The interrelation between vibrothermographic crack heating, crack size and vibrational stress was established. It was also found that both crack length and vibrational stresses increase crack heating.

The experimental work done by Renshaw [2] and Holland [3] substantiate the problem of repeatability in vibrothermography. Furthermore, this gives rise to another important question which has to do with the different factors contributing to this development. Due to the complexity involved with vibrothermography, different test specimens behave differently under the analysis. This is because each material has different resonant frequencies at which the best results are obtained. Moreover, factors such as crack length, orientation, coupling between transducer and specimen, etc. make it difficult to understand the exact governing physics behind heat generation during a vibrothermographic analysis. All the above-stated problems have made the vibrothermography technique unacceptable commercially. With advancement in technology, finite element analysis (FEA) has proven to be highly advantageous. The use of this tool reduces both the cost as well as the time required to replicate similar experimental procedures. A similar probability of a detection study performed experimentally requires a substantial amount of money. These high expenses are due to the high selling cost of the components required during the experimental procedure. FEA can replace these studies in the testing stage if a practical model is developed, which accurately characterize vibrothermography. Thus, FEA can be used to overcome the above-mentioned hurdles and get a better understanding of the method of vibrothermography. Hence, a framework is required to model the vibrothermographic process accurately. The objective of this research is to work upon the development of this template and characterize the process of vibrothermography, so that it becomes a step closer to be commercially accepted.

### **1.3. Research Contribution**

The contributions of this research work can be summarized as follows:

- Provides a deep insight into the development of a finite element model to aptly represent the process of vibrothermography.
- Explore in depth the role of meshing and its effect on frequency.
- Study the behavior of different crack sizes to characterize the physics behind the procedure.

#### **1.4. Thesis Organization**

The rest of the thesis is organized as follows: Chapter 2 provides a background on various factors that govern or affect the process of vibrothermography. Moreover, an insight into previous groundwork relevant to this topic is discussed. Chapter 3 discusses in depth the process of creating a finite element model to simulate vibrothermography. All the parameters governing the definition of a functioning model are explored and reported in this chapter. Chapter 4 establishes a theoretical model which analyzes the frequency effect on the strain value recorded during the process of vibrothermography. This theoretical model is developed mainly to validate a mesh convergence study done for a no crack model. Chapter 5 presents the formulization and results obtained from a modal and harmonic response analysis. The heat generation results are discussed in chapter 6. Finally, chapter 7 provides a conclusion to the thesis and lays out the prospected future work.

## Chapter 2. Background and Literature Review

This chapter aims to provide a broad understanding of the method of vibrothermography. Capturing the generated heat during a vibrothermographic simulation requires defining a number of parameters including specimen material and geometrical properties, wave dispersion, fracture mechanics, contact parameters, heat generation parameters, etc. Hence a deep understanding of each of them is necessary to carry out the analysis accurately. This section discusses the heat generation aspect of vibrothermography and the different factors that influence it. Doing this will help in achieving a better understanding of the process and will set a strong foundation for this research.

### 2.1. Types of Heating

The heat generation in vibrothermography can be attributed to one or more of the following:

**2.1.1. Frictional heating.** When the specimen under inspection is excited by a sonic transducer, the crack surfaces rub against each other and result in frictional heat generation. The heat generation due to friction does not occur past the crack tips since there are no surfaces in contact beyond that point. It was observed that 5% of the frictional energy generated during vibrothermography is absorbed by the material and accounts for microstructural changes and phase transformations [4]. The remaining 95% raises the temperature around the crack. The heat generated by friction,  $Q$  can be calculated using Equation (1).

$$Q = \mu N v \quad (1)$$

where  $\mu$  is the sliding friction coefficient,  $N$  is the normal applied force and  $v$  is the sliding velocity.

**2.1.2. Viscoelastic heating.** It is evident that viscoelastic heat is almost negligible in specimens made of metals. But it is a prominent factor for polymer-based composites [5]. It occurs mostly due to increased concentration of vibrational stresses at the crack interface. For any elastic material loaded with stress, the viscoelastic damping will result in a phase shift with that compared to a material with no viscoelastic damping. This will lead to the release of energy in the form of heat. Figure 2.1 shows the stress-strain curve when viscoelasticity is present (a) and not



present (b), within the elastic range. The energy released can also be calculated from the area under the curve shown in Figure 2.1. Equation (2) is used to calculate the viscoelastic heating occurring during the vibrothermography process.

$$Q = T \frac{\partial S}{\partial t} - \nabla(\lambda \nabla T) \quad (2)$$

where  $S$  is entropy,  $T$  is the average temperature,  $Q$  is the heat generation rate and  $\lambda$  is the thermal conductivity matrix.

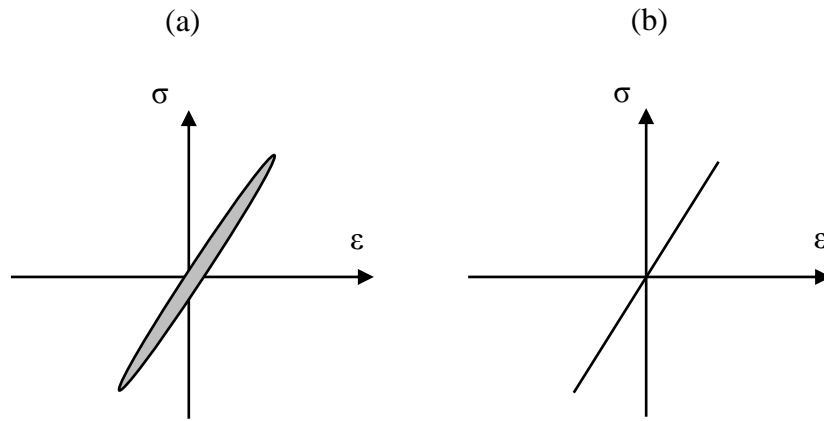


Figure 2.1: Stress-strain curve showing the difference between (a) viscoelastic material and (b) purely elastic material

To understand how viscoelastic heat is generated during a vibrothermographic analysis, Renshaw et al. [6] provided a method to create viscous material filled synthetic defects, which, similar to cracks, generate heat when the material containing them is stimulated with a sonic transducer. Several viscous materials were tested, where honey was selected as the most suitable one since it is easy to fill defects as well as give excellent heating patterns compared to others. This helps in understanding the capability of a vibration source to detect the defects present at different locations in an object. It was found that defects located at high vibrational stress regions generate more heat than those located at low vibrational stress regions. More work related to viscoelastic heating was done by Montanini et al. [7]. The main objective was to find an analogy between vibrational mode shape, ultrasound frequency and energy dissipation for regions containing defects. The experimental analysis was performed on a specimen with several viscous materials filled synthetic defects. Holes were created, and they were filled with honey [6]. The specimen was

excited by flexural resonant frequencies, and consecutively vibration and heating response were recorded. It was observed that the vibrating mode shape was an influential factor on the heating rate across the defect.

**2.1.3. Plastic heating.** Plastic deformation occurs when the applied vibrational stresses are more than the yield stress of the material. This plastic deformation occurs simultaneously with the generation of a large amount of heat. For a crack, there are higher stresses present near the crack tip due to the geometric stress intensity factors. This results in the growth of the crack due to plastic deformation at high loads. Also, the stresses at the crack tips increase with the crack length. Mabrouki et al. [8] conducted numerical and experimental analyses to understand how this plastic heat is generated. The natural frequencies and mode shapes were estimated via finite element simulations. The experimental work was done using the obtained data from the finite element model (FEM) for various crack lengths. The experiments validated the results that were obtained from the numerical model for the temperature distribution. It was also found that the stress at the crack faces exceeds the materials yield stress, thus proving that the heat generated during the analysis was due to plastic deformation.

Most of the early work on vibrothermography assumed that heat generation is a result of friction. Renshaw et al. [5] performed an experiment to get a better understanding of how exactly heat is generated during a vibrothermographic inspection. The author concluded that the principal source of heat generation can be attributed to frictional, viscoelastic and plastic heating depending on the material, vibrational stress level and type of defect. Equation (3) predicts the plastic heating during a vibrothermographic inspection process under conditions of uniaxial stress, using the following model:

$$\rho c \frac{\partial T}{\partial t} + \lambda \frac{\partial^2 T}{\partial x^2} = \beta \sigma \dot{\varepsilon}^p - \alpha E \frac{\partial^2 T}{\partial x^2} \varepsilon^e \quad (3)$$

where  $T$  is the absolute temperature,  $\sigma$  is the uniaxial stress,  $\varepsilon^e$  is the elastic strain,  $\varepsilon^p$  is the plastic strain,  $E$  is the Young's modulus,  $\rho$  is the mass density,  $c$  is material specific heat,  $\lambda$  is material thermal conductivity and  $\alpha$  is the thermal expansion coefficient.

## 2.2. Parameters Affecting Heat Generation

**2.2.1. Crack motion.** The motion of the crack is dependent on the frequency at which it is being vibrated. One can eliminate the variability of crack detection due to crack motion by understanding the actual motion of the part [9]. A crack under vibration can behave in a number of ways. Out of the many eigen modes, the three principal modes which show the motion of the crack are illustrated in Figure 2.2. For the tensile mode (Clapping), the crack faces are moving perpendicular to each other and hence generate almost negligible heating. The two remaining modes mainly contribute to the heat generation over the crack surfaces.

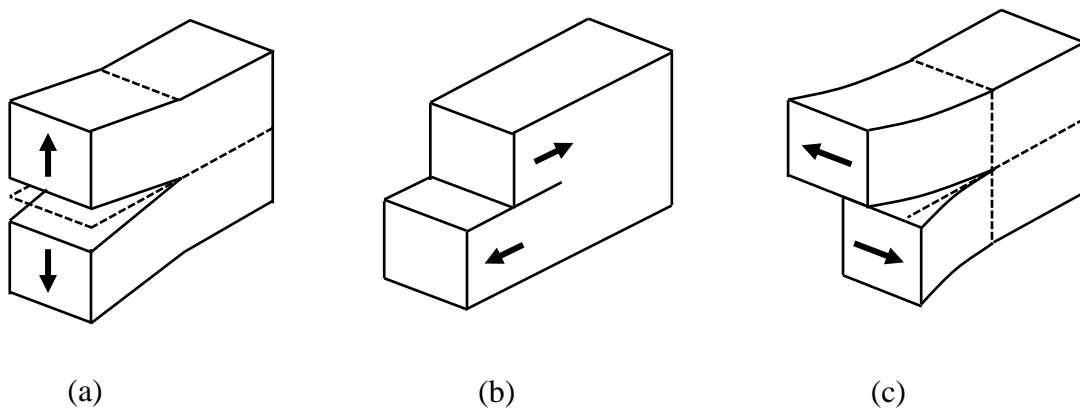


Figure 2.2: Three principal modes of vibration showing crack face motion (a) tensile mode (clapping), (b) in-plane shear mode (rubbing) and (c) anti-plane shear mode (tearing)

There are multiple ways used to detect the vibration mode of a specimen under inspection. One direct way is to measure the displacement at different surface areas on the specimen [10]. Though this is a highly accurate method, it is very time consuming and impractical for most of the cases. Another way to analyze the vibrational modes is by using FEM. FEM is excellent for estimating the mode shapes, but modelling the whole system is often time-consuming. For simple geometries, vibrational mode shapes can be estimated theoretically.

**2.2.2. Crack length.** The crack length has a direct effect on heat generation during a vibrothermographic analysis. Since frictional heat is generated when the crack faces rub against each other upon vibration, we can say that the longer the crack length is, the more heat will be generated. This is since a long crack will clearly have

more surface area in contact resulting in more frictional heat generation. The work done by Holland et al. [12] support the above concept regarding the crack size. The author performed experiments on titanium and Inconel samples to understand the above-stated effects. It was concluded that larger cracks developed more heat compared to the smaller ones. Thus, the paper provides a good insight into the correlation between crack heating and crack length. Another paper by Wong et al. [13] further enhances the above concept. An experiment was performed which involved cracks of different sizes. To limit variability, the input vibrations were kept constant for all experiments. Thus, it was found that for larger crack size, more heat was generated.

**2.2.3. Vibration power.** The power of the sonic transducer also plays a crucial role in the detection of cracks. If the power is too low, we will get low vibration amplitude, and therefore we may be unable to detect the crack. Most of the work done previously usually took a high-power sonic transducer to detect cracks. Furthermore, another factor to be considered is the nonlinear relation occurring due to the coupling between the transducer and the specimen [11]. Doing this increases the probability of detecting cracks, but it often leads to getting non-repeatable results. Moreover, the use of a high-powered transducer increases the chances of damaging the specimen.

Thus, it can be concluded that, in order to ensure crack detectability, it is essential that an appropriate amount of heat is generated over the crack surface. To demonstrate this, Holland et al. [12] worked on finding the relationship between resonant vibrational stresses and heat generation. The authors used a single frequency sonic transducer to get a particular resonant frequency. Doing this enabled them to understand the vibrational mode for the specimen they are using. Once the vibrational mode was established, the generated dynamic vibrational stresses were calculated. Several experiments were performed on titanium and Inconel samples to understand the above-stated effects. It was noticed that as the dynamic stresses increased, the crack heating also increased. Thus, the analysis provided a good insight into the correlation between crack heating and vibrational stresses.

**2.2.4. Acoustic chaos.** Generally, the sonic source used for analysis is a single frequency one, but the nonlinear coupling between the transducer and the

specimen can cause the occurrence of other frequency components that are multiple of rational fractions of the induced frequency. This is referred to as acoustic chaos. Various studies have shown that this acoustic chaos enhances the detection of defects going under a vibrothermographic inspection.

The above fact is fortified by the results obtained by Han et al. [11]. A series of experiments were performed. The crack size was kept constant throughout the experiments. Different couplant materials were used. Using different couplant materials induced chaotic vibration in some cases and harmonic vibration in others. It was found that acoustic chaos does enhance crack detection during a vibrothermographic inspection. To further get a better understanding of the physics behind this, Han et al. [14] implemented a finite element model to understand and calculate the energy that is dissipated during a vibrothermographic inspection over a cracked surface. For the case considered, it was inferred that due to the existence of acoustic chaos which occurs because of the nonlinear coupling between the transducer and specimen, better results were obtained. Due to acoustic chaos, many additional fractional wavelengths of waves are produced which resonate with the specimen and amplifies the heating.

**2.2.5. Crack closure.** Crack closure is defined as a case when the crack faces are in contact with each other in spite of the external forces acting over it. At this stage, the crack only opens when a particular stress threshold is crossed and overcome the static friction. Crack closure has a significant effect on heat generation. No heating would be observed if the compressive stresses are greater than the amplitude of the applied vibration since the vibrational stress incurred will not be able to overcome the static friction. Furthermore, when the crack faces are too far from each other, no heating would be observed along the crack, but might rather be generated at the crack tips [15].

To understand the effect of crack closure, Lu et al. [16] performed an experiment involving an aluminum specimen in which different closure stresses were achieved by using clamping devices. They concluded that due to the clamping force applied specifically to their case, less heat was generated over the crack surface. Additionally, Renshaw et al. [17] performed an experiment with titanium samples. Cracks with different closure states were grown. It was observed that larger and open

cracks generate more heat near the crack tips, while smaller and tighter cracks in comparison generate heat towards the crack center.

**2.2.6. Material properties.** The material of the specimen plays a crucial role in the generation and detection of heat. Some materials exhibit more viscoelastic heat generation than others. This affects the rate of defect detection since more heat is generated. Another factor that comes into play is the materials yield stress. If the material has low yield stress, plastic deformation may occur, and this needs to be avoided.

Xiaoyan Han et al. [18] investigated the effect of material properties on heat generation using FE simulations. Two alloys were considered, namely Aluminum and Titanium alloys. It was found that aluminum has higher acoustic energy than titanium.

### **2.3. System Setup**

Though an experimental setup has not been used in this research, this section aims at explaining the process of vibrothermography. Figure 2.3 shows a schematic representation of a sonic IR system, which includes:

1. **Sample:** Vibrothermographic analysis can be used for a number of versatile materials. Various test specimen materials that have been used for research purposes are Titanium, Carbon fiber composites, aluminum, etc.
2. **Sonic Transducer:** The transducer is used to vibrate the cracked specimen. Usually, a piezoelectric transducer is used, but in some cases magneto strictive devices are also used. Work done by X Guo et al. [20] shows that results obtained were very much similar in terms of detection of the crack. The specimen could be excited at predetermined frequencies such as 20 kHz, 30 kHz or 40 kHz, or at lower power arbitrary frequencies. A couplant is present between the transducer and the specimen. This couplant is usually for protecting the sample from getting damaged; it also helps on delivering the best coupling during the inspection.
3. **IR Camera:** IR cameras are used to monitor and detect thermal indications, where heat generated is due to the defects present in the sample.
4. **PC** is used for storing and managing the recorded data.

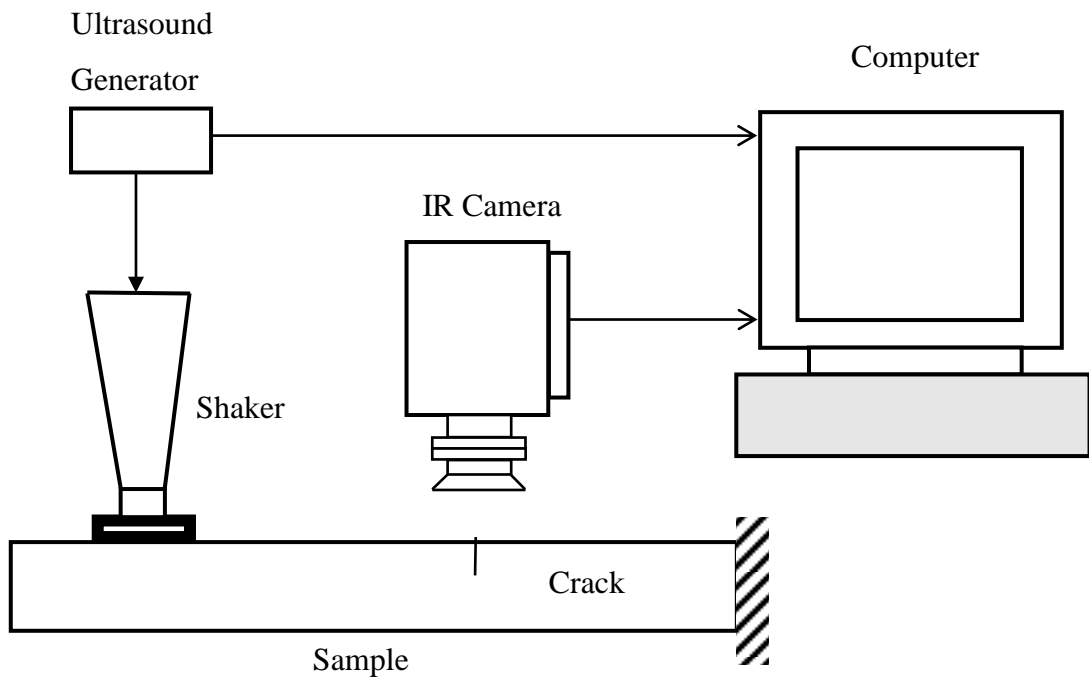


Figure 2.3: Schematic representation of a sonic IR system

### Chapter 3. Finite Element Modeling of Vibrothermography

Numerical modelling helps in understanding the underlying physical behavior of complex problems. It is convenient in assisting users in obtaining qualitative results in a time and cost-efficient manner. To accurately simulate a vibrothermographic system, one must know the effect the vibrational stress will have while propagating through the material. As it is known that the heat generation in a vibrothermographic system is usually due to the internal and external heat generation. Here are the constitutive laws governing these:

1. The external heat generation is mainly attributed to frictional rubbing of contacting crack surfaces under different vibrational modes. Equation (4) gives frictional heat generation for a finite element model and accurately portrays Equation (1) [21]. The total heat generated  $Q(t)$  in Equation (4) is the summation of heat generated at all the nodes  $N$  at the crack surface over a time interval  $t$ . In Equation (4),  $\mu_s$  is the static friction coefficient,  $\mu_d$  is the dynamic friction coefficient,  $c$  is a constant at which transition in velocity occurs,  $v_i$  represents the velocity for  $i_{th}$  element,  $p_i$  is the pressure between the  $i_{th}$  element and the one adjacent to it and  $\delta A_i$  is the area of the  $i_{th}$  element at the crack surface.

$$Q(t) = \sum_{j=0}^{t/\delta t} \sum_{i=1}^N \{[\mu_d + (\mu_s - \mu_d) e^{-c|v_i(t_j)|}] p_i(t_j) v_i(t_j) \delta A_i\} \delta t \quad (4)$$

2. The internal heat generation is attributed mostly to viscoelastic and plastic heat deformation. The viscoelastic heat generation occurs when the specimen under high-frequency vibration shows damping and eventually the vibration fades out. This results in the generation of viscoelastic heat. The viscoelastic heat generated can be calculated as the area under the stress-strain curve in Figure 2.1. The plastic heat generation occurs when the stress applied to the specimen is more than the yield stress of the material. This results in plastic deformation at the crack tip, and thus the generation of heat.

Numerous analyses have been performed by researchers to enhance their understanding of vibrothermography. Rizi et al. [21] used FEM for understanding the different aspects of the process. The analysis involved modelling a cracked specimen



and further identification of the different heat sources involved during the procedure. Two models were established one considering the effects of internal energy losses while the other considering external losses. The internal losses considered the viscoelastic and thermoplastic damping, while the external losses took into account the friction between the crack surfaces. Although the work of Rizi et al. provided a good understanding of the effects of the heat sources and the reliability of the method, it failed to address in detail the modelling aspect of the process. The relation between the amount of induced vibration and the related heat generation was also not investigated.

### 3.1. Stress Intensity Factor

Stress intensity factor (SIF) can be estimated theoretically or computationally to estimate the peak stress at the crack tip. This helps in predicting the failure criteria of the specimen under observation. The SIF varies with the size and location of the crack in a specimen. Even the different modes affect the SIF. Equation (5-7) are used to calculate SIFs theoretically for the three modes discussed in Section 2.2.1

$$K_I = \lim_{r \rightarrow 0} \sqrt{2\pi r} \sigma_{xx}(r, 0) \quad (5)$$

$$K_{II} = \lim_{r \rightarrow 0} \sqrt{2\pi r} \sigma_{yx}(r, 0) \quad (6)$$

$$K_{III} = \lim_{r \rightarrow 0} \sqrt{2\pi r} \sigma_{xz}(r, 0) \quad (7)$$

where,  $K_I, K_{II}$  and  $K_{III}$  are the stress intensity factors at the three modes,  $r$  is the distance from the crack tip and  $\sigma_{ij}$  is the stress component at the crack tip. Alternatively, the SIF can be calculated numerically using the following methods:

1. **The J-integral:** The J-integral technique considers the energy released during the process of crack extension [22]. It is primarily used for rate-independent quasi-static analyses. Equation (8) provides the general expression for calculating the J-integral.

$$\vec{J} = \int_{\Gamma} \left( W dy - \vec{e} \frac{\partial \vec{u}}{\partial x} ds \right) \quad (8)$$

where,  $\Gamma$  is the curve around the crack tip,  $e$  is the traction vector,  $u$  is the displacement vector,  $ds$  is a small arc length along  $\Gamma$  and  $W$  is the strain-energy density which is defined using Equation (9).

$$W = \int_0^\varepsilon \sigma_{ij} d\varepsilon_{ij} \quad (9)$$

where  $\sigma$  are the stresses,  $\varepsilon$  are the infinitesimal strain tensors,  $i$  and  $j$  represent the components in the  $x$  and  $y$  axes respectively.

2. **Crack extension:** Another way to calculate the SIF at the crack tip nodes is to use the concept of crack extension; this is achieved by using one of the following criteria:
  - a. Maximum Tangential Stress (MTS) criterion [23] uses the fact that the crack extension direction is considered as that of the MTS, where the SIF is calculated based on the result obtained for the propagation direction.
  - b. Maximum Energy Release Rate (MERR) criterion [23], where the crack extension direction along the maximum energy release per unit extension is taken as the direction of maximum SIF.
  - c.  $K_{II} = 0$  criterion [22] assumes that the initial direction of crack extension is that of  $K_{II} = 0$ .

Numerical analysis for vibrothermography involves performing a thermal analysis to understand the heat generation and transfer around the crack. Any study in the field of fracture mechanics pertaining to cracks results in the occurrence of a singularity at the crack tip. Meshing plays a crucial role in capturing the physics at the crack tip to obtain accurate results. Accordingly, selecting the right element type and meshing criteria are essential to analyze the convergence of the solution for a specific application. To understand the effect of mesh on SIF, a model similar to Figure 3.1 is created in ABAQUS. Using a fine enough mesh will give a convergent solution for most parts of the bar except at the crack tip, where singularity is present.

To overcome the singularity at the crack tip, wedge shape elements whose middle node is shifted towards the quarter position need to be used, as shown in Figure 3.2. Figure 3.3 shows a meshed model in ABAQUS. Figure 3.4 shows the meshed pattern around the crack tip. It includes wedge shape elements at the center of the circle.

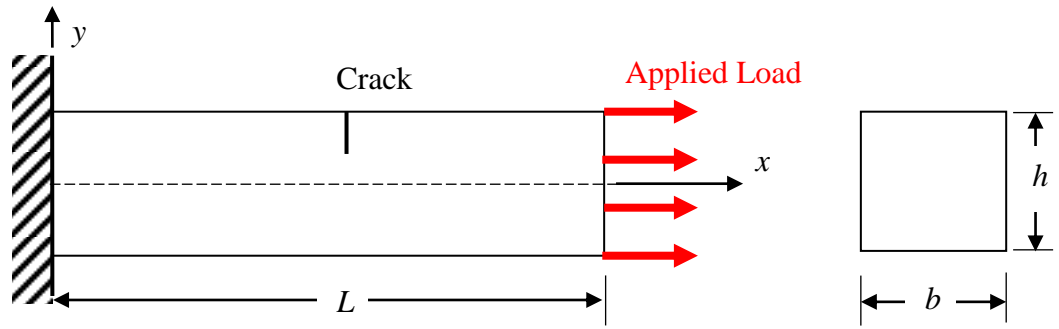


Figure 3.1: Schematic representation of the model used for estimating SIF ( $K_I$ ) at the crack tip

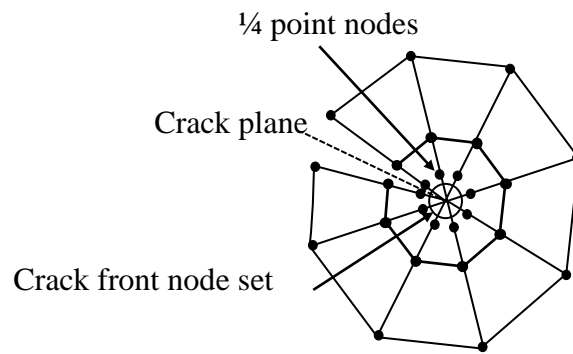


Figure 3.2: Schematic of the quarter node wedge shape elements around a crack tip

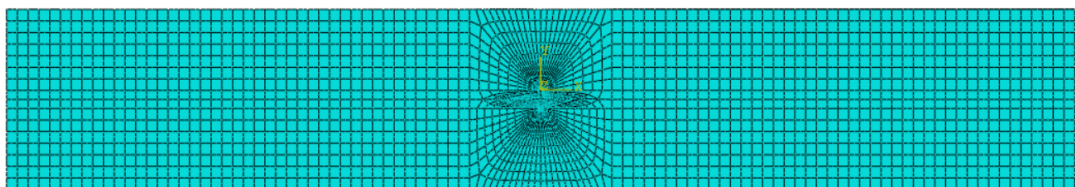


Figure 3.3: Meshed model created in ABAQUS with quarter node wedge shape elements at the crack tip

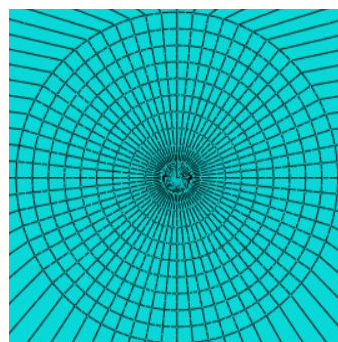


Figure 3.4: Close up view of the crack tip showing the circular fan mesh

But for modelling a vibrothermographic process in ABAQUS, a heat generation analysis which does not allow the use of quarter node wedge shaped element at the crack tip is necessary. Hence, a normal wedge-shaped element is used instead and verified in Chapter 6.

Schematic shown in Figure 3.1 is modelled with different meshes in ABAQUS. These meshes have been described later in Section 3.8. To calculate the SIF, the method  $K_{II} = 0$  has been used. Figure 3.5 shows the SIF at the crack tip when the bar is under mode-I loading. It can be seen that when the element size is decreased, the least variation in SIF value is observed in the quarter node wedge mesh and the circular mesh. While for the rectangular and semi-circular mesh, the stress intensity factor is rapidly changing with decreasing mesh size. Furthermore, the SIF for the quarter node wedge shape element is beginning to converge with the calculated theoretical solution for the finest mesh. Thus, due to the above stated limitation, the singularity cannot be completely avoided in a thermal analysis. However, its effect is limited if a circular mesh is used.

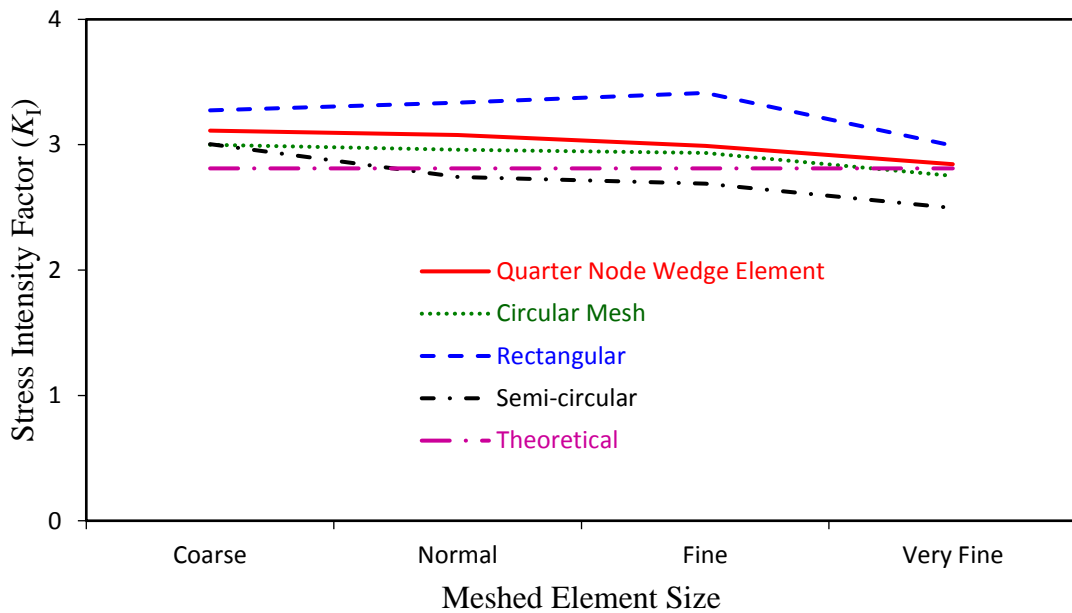


Figure 3.5: The effect of selecting the element type and meshing criteria in estimating the SIF ( $K_I$ )

### 3.2. Proposed Model Design

A FE model was created in ABAQUS. The model consisted of a rectangular bar of dimensions 300 mm × 15 mm × 15 mm. The material selected for the bar is Medium Carbon Steel. A thorough crack was created in the center of various sizes. The crack sizes modelled were between 2 and 6 mm in depth with 1 mm increments. The crack was modelled in such a manner that a discontinuity was created between the two crack surfaces. This meant that when at rest, the two surfaces of the crack are in complete contact with one another and no other material is present between them. Table 3.1 shows the material properties considered for the analysis.

Table 3.1: Medium carbon steel material properties used in ABAQUS

Material properties	Value
Density ( $\rho$ )	7800 kg/m <sup>3</sup>
Modulus of Elasticity ( $E$ )	200 GPa
Poisson's Ratio ( $\nu$ )	0.3
Thermal Conductivity ( $\lambda$ )	43 W/m-K
Specific Heat ( $C_p$ )	0.490 J/g-°C

### 3.3. Damping

During kinematic analysis, the damping of a system under any kind of harmonic or vibrational loading is often estimated. Nevertheless, the problem of damping becomes an indispensable issue when dealing with continuously vibrating systems. It becomes difficult to estimate the value of damping which befits the system in its entirety. Hence, to understand the effect damping had on the system, there is need for developing a profound understanding of the concept. Since all our work is based on FEA, the first step includes understanding the ways one can define damping in ABAQUS.

FEA software such as ABAQUS provides multiple ways to implement damping in an analysis [22]. The most common way is the use of Rayleigh damping.

Other methods include defining dashpots, inelastic material behavior, etc. Rayleigh damping, being generic in nature, is more advantageous in many cases including analysis pertaining to lower and higher frequency range behavior.

FEA software, such as ABAQUS, provides multiple ways of implementing damping in an analysis [22]. The most common way is the use of Rayleigh damping. Other methods include defining dashpots, inelastic material behavior, etc. Rayleigh damping, being generic in nature, is more advantageous in many cases including analysis pertaining to lower and higher frequency range behavior.

Rayleigh damping comprises of two damping factors, namely  $\alpha_R$  which signifies the mass proportional damping and  $\beta_R$  which characterizes the stiffness proportional damping. The expression for damping ratio  $\xi_i$  for any mode  $i$  in terms of  $\alpha_R$  and  $\beta_R$  is given in Equation (10).

$$\xi_i = \frac{\alpha_R}{2\omega_i} + \frac{\beta_R\omega_i}{2} \quad (10)$$

where  $\omega_i$  is the natural frequency at this mode. It can be inferred from Equation (10) that the mass proportional damping parameter affects the lower frequencies, while the stiffness proportional damping parameter affects the higher.

In ABAQUS, the mass proportional damping factor  $\alpha_R$  mimics the effect an object has when moving through a hypothetical viscous fluid. The fluid is so assumed that damping takes place at every occurrence of motion [22]. The stiffness proportional damping factor  $\beta_R$  creates a damping effect that is directly dependent on the elastic material stiffness. Thus, it produces damping that is dependent on the strain rate of the material.

There are no experimental procedures through which one can directly determine the value of the two damping factors. But an accurate measurement can be made using damping ratio  $\xi$ . The damping ratio can be calculated using many procedures such as the half-power bandwidth method [11]. On obtaining this value, the damping factors  $\alpha_R$  and  $\beta_R$  can be calculated using modal frequencies. The modal frequencies can be estimated using ABAQUS, by doing a modal analysis. The value of  $\alpha_R$  and  $\beta_R$  is estimated using Equation (11) and (12)

$$\alpha_R = 2 \xi \frac{\omega_p \omega_q}{\omega_p + \omega_q} \quad (11)$$

$$\beta_R = \frac{2 \xi}{\omega_p + \omega_q} \quad (12)$$

where  $\xi$  is the average of  $\xi_p$  and  $\xi_q$ ,  $p$  and  $q$  denote the  $p^{\text{th}}$  and  $q^{\text{th}}$  modal frequency.

Since the nature of our analysis is explicit, ABAQUS offers another method to control damping for such an analysis. A sufficient quantity of damping is set forth in the form of bulk viscosity that impacts high-frequency oscillations. Bulk viscosity is subdivided into two parts: linear and quadratic bulk viscosities.

Linear bulk viscosity [22] is present in each element of the mesh. It has a linear effect on the volumetric strain rate. This damping is also called as truncation frequency damping. The linear bulk viscosity ( $p_{bv1}$ ) can be calculated using Equation (13).

$$p_{bv1} = b_1 \rho c_d L_e \dot{\epsilon}_{vol} \quad (13)$$

where  $b_1$  is linear damping coefficient,  $\rho$  is density,  $c_d$  is the current dilatational wave speed,  $L_e$  is an element characteristic length and  $\dot{\epsilon}_{vol}$  is the volumetric strain rate.

Quadratic bulk viscosity [22] is present in solid continuum elements. It has a quadratic effect on the volumetric strain rate. The quadratic bulk viscosity ( $p_{bv2}$ ) can be calculated using Equation (14).

$$p_{bv2} = \rho (b_2 L_e \dot{\epsilon}_{vol})^2 \quad (14)$$

where  $b_2$  is quadratic damping coefficient,  $\rho$  is density,  $L_e$  is an element characteristic length, and  $\dot{\epsilon}_{vol}$  is the volumetric strain rate.

**3.3.1. Effect of damping on stable time increment.** The stable time increment is inversely proportional to the critical damping ratio. Thus, if the critical damping ratio decreases, the stable time increment will increase. This relation is governed by Equation (15).

$$\Delta t \leq \frac{2}{\omega_{max}} \left( \sqrt{1 + \xi_{max}^2} - \xi_{max} \right) \quad (15)$$

where  $\omega_{max}$  is the frequency of the highest mode,  $\xi_{max}$  can be calculated using Equation (16). Hence, we get Equation (16) by substituting  $\omega_{max}$  in Equation (15).

$$\xi_{max} = \frac{\alpha_R}{2\omega_{max}} + \frac{\beta_R\omega_{max}}{2} \quad (16)$$

Equation (15) and (16) indicate that stiffness proportional damping  $\beta_R$  has a considerable outcome on stable time increment than the mass proportional damping  $\alpha_R$ .

In this research, the method of bulk viscosity was used to implement damping in the model. A trial and error based analysis was done by keeping the step time increment constant and varying the linear and bulk viscosities. It was found that the quadratic bulk viscosity did not have much effect on the analysis, while the monitored values varied with changes in the linear bulk viscosity alone. This was done until temperature values were in accordance to the work done by Morbidini et al [24]. Hence, based on this, the linear bulk viscosity value ( $b_1$ ) was set to 0.03 and the quadratic bulk viscosity ( $b_2$ ) was kept at the default value of 1.2.

### 3.4. Friction

Since frictional heating is the main heat generation source in our case, an elaborate frictional heating model needs to be applied in ABAQUS to record the heat generated over the designed crack in our model. The default friction model in ABAQUS is the coulomb friction model. The coulomb friction takes a quasi-static approach and defines the generated heat to be dependent on the velocity-force correlation. Prior work has led to the conclusion that heat generated due to friction is not only based on force-velocity correlation but also on the rate of velocity change. It has been exhibited as well that the displacement also has a crucial effect on the generated heat. Due to this, there is often an anticipated lag in response to the change of forces on the body under motion.

Though the coulomb friction model has many advantages, it does not consider the acceleration present between elements that are in contact with each other. Many other frictional contact models are available that may define the frictional interactions more properly. Examples of such models are the LuGre model and the Leuven model [25]. In this research, the coulomb friction model has been selected for the analysis of frictional heat. Despite its limitation, the coulomb friction model is adequate to represent the case of vibrothermography assumed in this research. Furthermore, the



parameters involving frictional behavior definition are prominently available in numerous scholarly works [4,21]

In ABAQUS, the coulomb friction model compares the maximum shear stress occurring across the contact surface to the pressure developed between them. Based on this, it decides whether the contact surfaces are in relative motion with one another. Before a particular strain magnitude is achieved, the surfaces under contact remain at rest. This is called the critical shear stress. The critical shear stress is expressed using Equation (17), it is directly proportional to the contact pressure between the surfaces in contact.

$$\tau_{crit} = \mu p \quad (17)$$

where  $\mu$  is the static friction coefficient and  $p$  is the pressure between surfaces. Equation (17) determines the point when the transition between sticking to sliding occurs.

To ensure an efficient coulomb friction model, it is essential that analysis be accurately designed as per our requirements. The need to properly define the behavioral model for the interaction is necessary to overcome any irregularities in the results. Since there is a static dependency between the force and velocity in a time domain, to adequately judge the generated friction heat, the time domain needs to be divided into smaller steps. A fine discretization in time will ensure that the frictional heat generated over the crack is accurate.

**3.4.1. Friction coefficient.** Now that a basic friction model has been decided, the next step is to choose the parameters that govern it. Most of the previous scientific research has used aluminum as the material for analysis [5, 14, 18, 21]. Researchers have chosen the dynamic coefficient value to lie anywhere between 0.25 to 0.4. Since not much work has been done to clearly identify the frictional coefficient value for steel to steel crack surface contact, 0.3 was selected in this study. ABAQUS provides two ways to define a coulomb friction model. The first way is to defines the friction coefficient as a function of contact pressure. The other way is to define static, dynamic and decay coefficients directly. In the default model, the friction coefficient is defined using Equation (18).

$$\mu = \mu(\dot{\gamma}_{eq}, p, \bar{\theta}, \bar{f}^\alpha) \quad (18)$$

where,  $\dot{\gamma}_{eq}$  is the equivalent slip rate,  $p$  is the contact pressure,  $\bar{\theta} = \frac{1}{2}(\theta_A + \theta_B)$  is the average temperature and  $\bar{f}^\alpha = \frac{1}{2}(f_A^\alpha + f_B^\alpha)$  which is the average predefined field variable.  $A$  and  $B$  refer to nodes on the two contacting surfaces. By default, the field variables do not contribute to the definition of the coefficient of friction. In this research, this method was used to define the coulomb friction model. The coefficient of friction has been selected to be 0.3.

The second method includes specifying the static, kinetic and the decay coefficients for the coulomb friction model. Equation (19) governs this relation.

$$\mu = \mu_k + (\mu_s - \mu_k)e^{-d_c \dot{\gamma}_{eq}} \quad (19)$$

where,  $\mu_k$  is the kinetic friction coefficient,  $\mu_s$  is the static friction coefficient,  $d_c$  is the decay coefficient and  $\dot{\gamma}_{eq}$  is the slip rate.

Table 3.2 displays the additional material properties that have been defined for the model. These include the damping coefficient as well as various thermal properties and frictional coefficients. These, together with to the material properties, are discussed in Section 3.2.

Table 3.2: Mechanical damping properties

Properties	Value
Damping (Linear), $\mathbf{b}_1$	0.03
Frictional Coefficient, $\mu$	0.3

### 3.5. Explicit Dynamic Analysis

Explicit dynamic analysis is an efficient tool provided in ABAQUS. It solves large problems by executing an ample number of small-time steps. The explicit dynamic analysis uses a numerical integration method called the central difference time integration to solve any model under consideration. The kinematic attributes can be calculated using Equation (20) and (21).

$$\dot{u}_{(i+\frac{1}{2})}^N = \dot{u}_{(i-\frac{1}{2})}^N + \frac{\Delta t_{(i+1)} + \Delta t_{(i)}}{2} \ddot{u}_{(i)}^N \quad (20)$$

$$u_{(i+1)}^N = u_{(i)}^N + \Delta t_{(i+1)} \dot{u}_{(i+\frac{1}{2})}^N \quad (21)$$

where  $N$  is the node under observation,  $u^N$  is a degree of freedom,  $i$  refers to the step time increment in the dynamic explicit analysis and  $\dot{u}^N$  &  $\ddot{u}^N$  are the first and second derivatives of  $u^N$ . As is in the case of any explicit analysis, the kinematic attributes for the next step are calculated based on the values of  $\dot{u}_{(i-\frac{1}{2})}^N$  and  $\ddot{u}_{(i)}^N$ , which were determined in the previous step time increment.

As previously mentioned, an element mass matrix is required to solve a dynamic explicit analysis. These are necessary to achieve computational efficiency in the analysis, which is not possible by using the central difference time integration alone. The initial acceleration is determined using the element mass matrix, which can be seen in Equation (22).

$$\ddot{u}_{(i)}^N = (M^{NJ})^{-1} (P_{(i)}^J - I_{(i)}^J) \quad (22)$$

where  $J$  represents the number of columns in the matrix  $M$ ,  $M^{NJ}$  is the mass matrix,  $P^J$  is the applied load vector and  $I^J$  is the internal force vector.

### 3.6. Stability

Stability is essential in any proposed solution. As we saw, the dynamic explicit analysis in ABAQUS uses the central difference time integration numerical method to solve the model subject to consideration. This analysis is conditionally stable, and stability only occurs when certain conditions are met. When no damping is present in the system, the stability is dependent on the highest frequency ( $\omega_{max}$ ) present in the system. It is determined using Equation (23).

$$\Delta t \leq \frac{2}{\omega_{max}} \quad (23)$$

If damping is present in the system, then the stability is given using Equation (24).

$$\Delta t \leq \frac{2}{\omega_{max}} \left( \sqrt{1 + \xi_{max}^2} - \xi_{max} \right) \quad (24)$$

where  $\xi_{max}$  is the damping ratio at the highest modal frequency.

**3.6.1. Stable time increment.** Computational stability is mostly exhibited using a stable time increment, which is defined as the time taken by the dilatational wave to cross the smallest element in the mesh. Thus, stable time increment is directly proportional to the element size in a mesh. Equation (25) approximates the stability time increment in ABAQUS.

$$\Delta t \approx \frac{L_{min}}{C_d} \quad (25)$$

where  $\Delta t$  is the stable time increment,  $L_{min}$  is the smallest element dimension and  $C_d$  is the dilatational speed across the smallest element.

Since the value of the stable time increment is approximated, usually in ABAQUS a safety factor is added to the model to ensure the accuracy of analysis. For 2D models, the estimated time increment will be reduced by a factor lying between  $\frac{1}{\sqrt{2}}$  and 1. Similarly, for a 3D model, the factor lies between  $\frac{1}{\sqrt{3}}$  and 1. Apart from this, stiffness accounted due to contact also contributes to the estimate of stable time increment.

**3.6.2. Dilatational wave speed.** The dilatational wave speed for any isotropic material is defined using Equation (26).

$$C_d = \sqrt{\frac{E(1-\nu)}{\rho(1+\nu)(1-2\nu)}} \quad (26)$$

where,  $E$  is the material's Modulus of elasticity,  $\nu$  is the Poisson's ratio and  $\rho$  is the density of the material. For our model, we have defined mild steel as the material. Its material properties are  $E = 200$  GPa,  $\rho = 7800$  Kg/mm<sup>3</sup> and  $\nu = 0.3$ . Thus, we can calculate the dilatational speed using Equation (26).

$$C_d = 5875.09 \text{ m/s}$$

Based on the dilatational speed, stable time increment can be approximated. But the value obtained using Equation (26) will not include other factors such as damping and contact. In this research, the stable time increment considered was based on that calculated by ABAQUS automatically. For most cases, it was approximated to 0.07  $\mu$ s and reduced for certain cases with finer mesh.

### 3.7. Contact

Another factor contributing to the reliability of the analysis is the contact definition between the crack surfaces. ABAQUS allows contact to be addressed in two ways. The first way is called the general contact, and the second is by defining contact pairs. In general contact, the contacting surfaces in the whole model are governed using single contact parameters. This results in all contacting surfaces tend to behave similarly over the course of the analysis. However, the other method involves defining the two surfaces which are in contact with each other and then the parameters that govern the physical relationship between them. Using the second method has the added advantage of assigning different contact parameters for different contacting surfaces.

Since the used model only analyzes a single crack, the general contact method has been used to interpret the interaction between the crack surfaces. Not having much difference between the two methods, the decision between them is based on both the number of contact surfaces as well as the processing time of the analysis. Due to the use of fewer parameters, the general contact method results in the consumption of less computational time and is therefore considered advantageous in terms of processing time.

**3.7.1. Surface properties.** The surface properties play an integral part in establishing a contact definition over surfaces. It can be clearly observed that these properties are a cardinal part of the contact interaction. Though the process to define a contact in ABAQUS is seen in Section 3.7, the physics that govern the required behavior is built based on the parameters of the surface properties. Hence to capture the frictional heating effect over the crack surface, the following surface properties need to be defined:

1. Tangential behavior: This property accounts for the tangential movement between the surfaces in contact. Since friction is the main tangential component, it is defined as discussed in Section 3.2.
2. Normal behavior: This property accounts for the normal movement between the contact surfaces. This is necessary so that the two contacting surfaces do not amalgamate during analysis. In this research, a pressure overclosure of “Hard” contact is defined.

3. **Thermal Conductance:** This property governs the thermal conductance occurring between the surfaces. When under harmonic motion, the model occasionally reaches a state where there is a gap between the two surfaces in contact. To govern this physical process, thermal conductance is defined. For our work, the thermal conductance was defined using pressure dependency data. Based on several trial analysis, the values of properties, as displayed in Table 3.3, were selected.
4. **Heat generation:** This property governs the amount of energy that is converted into frictional heat during the analysis. This value was set 0.95 [4]. The amount of heat distributed to each surface is set to 0.5.

Table 3.3: Surface properties: thermal conductance parameters

<b>Conductance [W/m-K]</b>	<b>Pressure [Pa]</b>
1000	0
1000	1000

### 3.8. Meshing

Meshing is the process of dividing the model into smaller parts called elements. It is a critical process for solving any finite element model. The model needs to be meshed into small elements until a convergence in results is achieved. The elements used in this research are of the type C3D8RT. Three profiles of meshes are generated for the bar.

1. **Rectangular Mesh:** This mesh consists of structural hexahedral C3D8RT elements of the same size throughout the model. Figure 3.6 (a) shows the bar created with a rectangular mesh. The main problem with such a mesh is that the results obtained through it are always higher than the anticipated values.
2. **Semi-circular Mesh:** This mesh consists of structural hexahedral C3D8RT as well as wedge-shaped C3D6T elements. A semi-circular shaped mesh is created along the surface of the crack, similar to a fan. The main problem with such a mesh is that it fails to account for the singularity at the crack tip. As seen in Section 3.1, the most critical part of a crack is its tip since the solution

never converges at this point. Hence, the mesh fails to solve this issue. Figure 3.6 (b) shows the semi-circular mesh.

3. Circular Mesh: As stated in Section 3.1, the best mesh to overcome the convergence problem at the crack tip is the one which creates a fan type structure around it. However, due to the limitation of the software to create a quarter node wedge-shaped element around the crack tip for thermal analysis, a normal wedge-shaped element is used instead. This mesh again consists of structural hexahedral C3D8RT as well as wedge-shaped C3D6T elements. Figure 3.6 (c) shows the created mesh. Figure 3.7 shows the close-up view of around the crack for all the three meshes discussed.

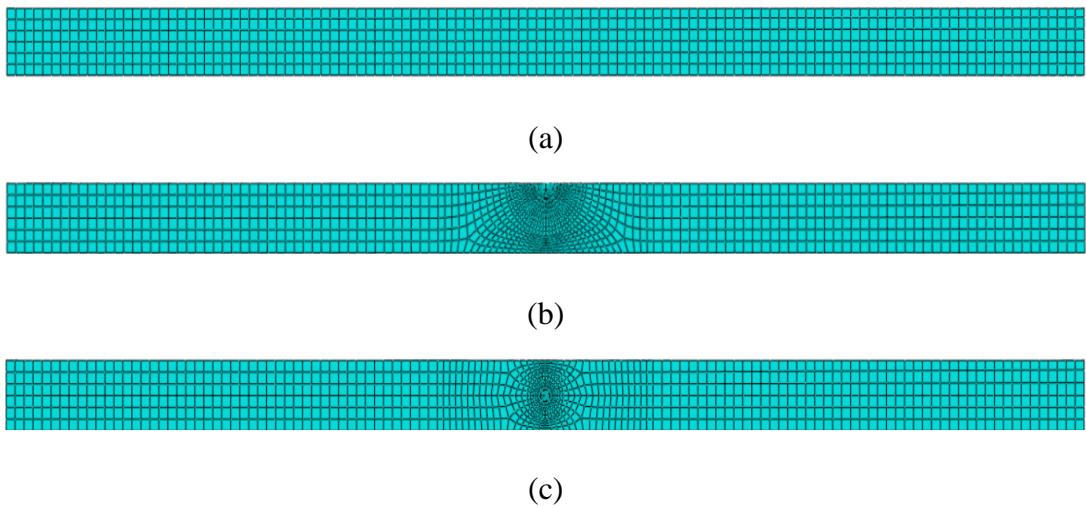


Figure 3.6: The proposed design model meshed using (a) rectangular mesh, (b) semi-circular mesh and (c) circular mesh

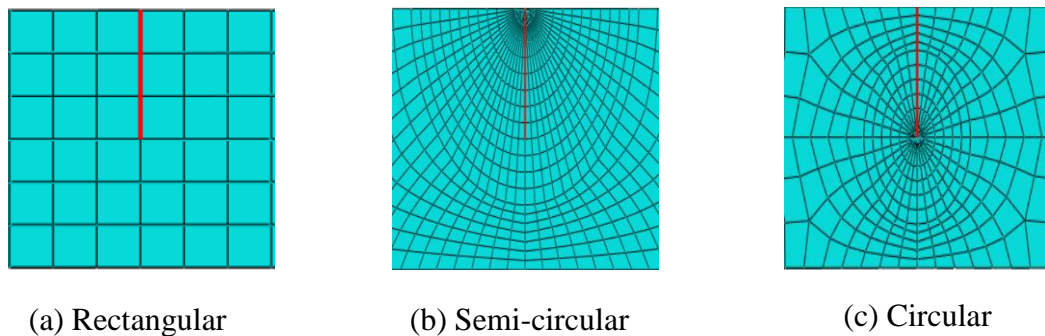
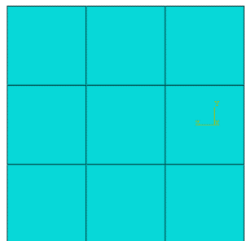
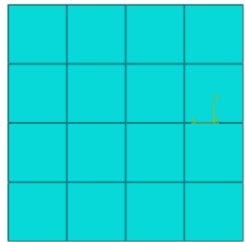
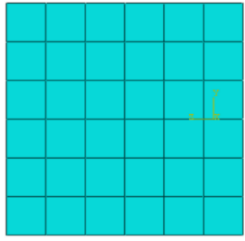
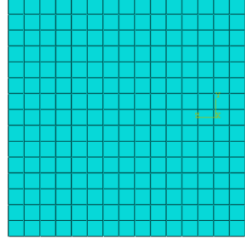


Figure 3.7: Close up view of the mesh around the crack

Table 3.4 discusses the four element sizes considered in this research. To study the effect of mesh completely, the bar is meshed with elements of different sizes. These sizes are classified as coarse, normal, fine and very fine, with cross-sectional views shown in the table as well.

Table 3.4: Mesh classification showing a cross-sectional view of meshes with different element sizes

Mesh classification	Element size [mm]	Total number of elements	Number of elements in cross-section	Cantilever beam cross-section view
Coarse	5.00	540	3×3	
Normal	3.75	1280	4×4	
Fine	2.50	4320	6×6	
Very Fine	1.00	67500	15×15	

### 3.9. Load, Boundary and Initial Conditions

To completely define the problem, appropriate loading and boundary conditions were defined. Figure 3.8 shows the load and boundary conditions applied



in ABAQUS. It can be observed from Figure 3.8 that the left side of the beam is completely fixed in all degree of freedoms. A sinusoidal displacement load is applied in the right-hand side. The sinusoidal load can be expressed using Equation (27).

$$U(y) = 0.002[\sin(2\pi 3000t) + \sin(2\pi 6000t) + \sin(2\pi 12000t) + \sin(2\pi 24000t)] \quad (27)$$



Figure 3.8: Load and boundary conditions applied on the model under analysis

Equation (27) shows the load as a combination of different frequency components, namely 3, 6, 12 and 24 kHz. This was used during the harmonic response analysis of the research. The load amplitude was selected so as to get acceptable strain readings for the finest model. For the heat generation analysis, only a single frequency was used, 24 kHz. The load amplitude for this analysis was selected to be 0.011 mm or 11  $\mu\text{m}$ . This selection was based on trial and error done with 5 mm crack size model. The amplitude was selected when an acceptable temperature value was registered based on the analyzed model. The model had the finest mesh amongst others.

Apart from the boundary conditions, the following assumptions were used:

1. Heat transfer occurs only through conduction. Convection and radiation heat transfer was not considered.
2. Temperature has no effect on the material properties.
3. Initially, the model is at the surrounding temperature.

## Chapter 4. Theoretical Solution

To assess the mesh size in delivering the surface strains as a function of frequency, it is assumed that the material is entirely uniform without any cracks. A theoretical model is established based on this assumption subjected to the loading conditions discussed in Section 3.9. This will estimate the largest element size needed for accurate wave propagation. Figure 4.1 shows a schematic representation of the defined model.

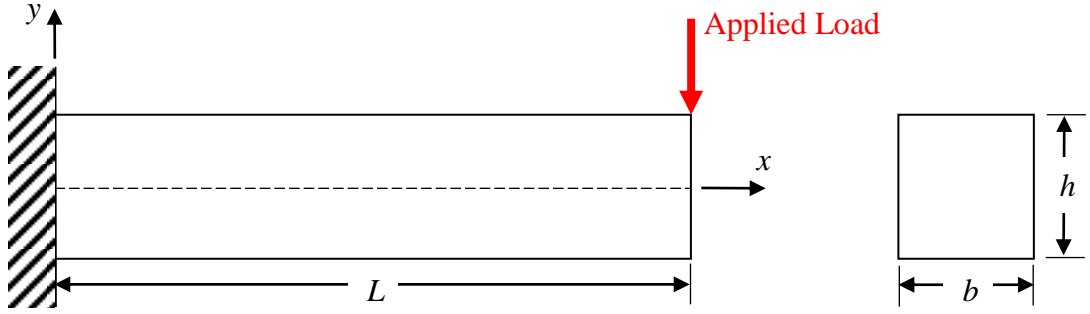


Figure 4.1: Schematic representation of the theoretical model

The model can be mathematically formulated using the following simple differential Equation (28).

$$IE \frac{\partial^4 v}{\partial x^4} = -\rho A \frac{\partial^2 v}{\partial t^2} \quad (28)$$

where  $I = \frac{1}{12}bh^3$  is the area moment of inertia for the rectangular bar,  $v$  is the displacement in the  $x$  direction,  $E$  is the modulus of elasticity,  $\rho$  is the density,  $A$  is the cross-sectional area, with width  $b$  and height  $h$ .

Substituting  $v = Ce^{i(\hat{k}x - \omega t)}$  in Equation (28) and simplifying, results in Equation (29)

$$\hat{k} = \pm\sqrt{\pm 1}k \quad \rightarrow \quad \hat{k}_{1,2} = \pm k \quad \text{and} \quad \hat{k}_{3,4} = \pm ik \quad (29)$$

where  $k = \sqrt[4]{\frac{12\rho\omega^2}{h^2E}}$ ,  $\omega = 2\pi f$  is the angular frequency and  $f$  is the frequency of the applied load.

Substituting values of  $\hat{k}$  in  $v = Ce^{i(\hat{k}x - \omega t)}$  results in Equation (30)

$$v = [C_1 \sin(kx) + C_2 \cos(kx) + C_3 \sinh(kx) + C_4 \cosh(kx)]e^{-i\omega t} \quad (30)$$

The boundary conditions governing the differential equation are mentioned in Equation (31-34).

$$v(0, t) = 0 \quad (31)$$

$$\frac{\partial v}{\partial x}(0, t) = 0 \quad (32)$$

$$\frac{\partial^2 v}{\partial x^2}(L, t) = M(L, t) = 0 \quad (33)$$

$$v(L, t) = ae^{-i\omega t} \quad (34)$$

Applying these boundary conditions to Equation (30) delivers a system of independent set of equations.

$$\begin{bmatrix} 0 & 1 & 0 & 1 \\ 1 & 0 & 1 & 0 \\ -\sin(kL) & -\cos(kL) & \sinh(kL) & \cosh(kL) \\ \sin(kL) & \cos(kL) & \sinh(kL) & \cosh(kL) \end{bmatrix} \begin{bmatrix} C_1 \\ C_2 \\ C_3 \\ C_4 \end{bmatrix} = \begin{bmatrix} 0 \\ 0 \\ 0 \\ a \end{bmatrix} \quad (35)$$

Solving the system in Equation (35) gives us the displacement  $v(x, t)$  as follows

$$v(x, t) = [C_1(\sin(kx) - \sinh(kx)) + C_2(\cos(kx) - \cosh(kx))]e^{-i\omega t} \quad (36)$$

$$C_1 = \frac{[\cos(kL) + \cosh(kL)]}{[\sin(kL) - \sinh(kL)][\cos(kL) + \cosh(kL)] - [\sin(kL) + \sinh(kL)][\cos(kL) - \cosh(kL)]} a \quad (37)$$

$$C_2 = \frac{-[\sin(kL) + \sinh(kL)]}{[\sin(kL) - \sinh(kL)][\cos(kL) + \cosh(kL)] - [\sin(kL) + \sinh(kL)][\cos(kL) - \cosh(kL)]} a \quad (38)$$

where  $C_1$ ,  $C_2$ ,  $C_3$  and  $C_4$  are 4 arbitrary constants in a general solution,  $x$  is the spatial coordinate,  $t$  is time,  $a$  is the amplitude of the applied load and  $L$  is the length of the bar.

The theoretically estimated displacement can be converted into strain using Equation (39).

$$\varepsilon = -\frac{y}{\rho_c} \quad (39)$$

where  $y$  is the distance from the longitudinal axis,  $\varepsilon$  is the longitudinal strain and  $\rho_c$  is the radius of curvature. The radius of curvature can be calculated using Equation (40).

$$\rho_c = \frac{\left[1 + \frac{dv^2}{dx}\right]^{\frac{3}{2}}}{\left|\frac{d^2v}{dx^2}\right|} \quad (40)$$

On substituting derivatives of Equation (36) in Equation (40), we get Equation (41).

$$\rho_c = -e^{-i\omega t} \left[ \frac{(k^2 e^{-2i\omega t} (C_1 \cosh(kx) - C_1 \cos(kx) + C_2 \sin(kx) + C_2 \sinh(kx))^2 + 1)^{\frac{3}{2}}}{(k^2 (C_2 \cos(kx) + C_2 \cosh(kx) + C_1 \sin(kx) + C_1 \sinh(kx)))} \right] \quad (41)$$

Upon solving the established theoretical model in MATLAB, a set of complex values are obtained. Figure 4.2 plots the absolute of these complex values when subjected to a wave amplitude ( $a$ ) value of -0.002. Also,  $y$  is set to half the height of the plate. These values are calculated at  $x = 150$  mm.

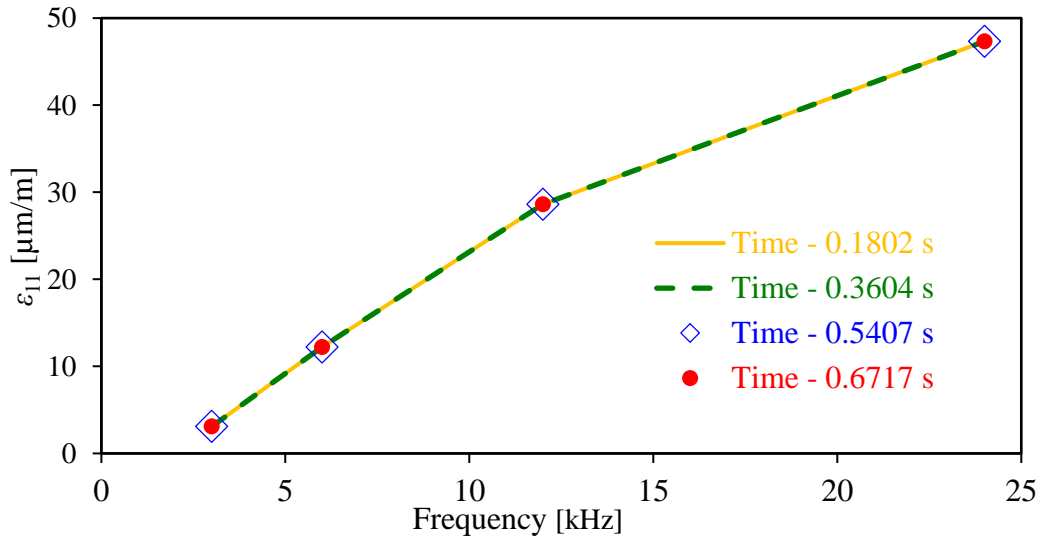


Figure 4.2: Theoretical solution obtained upon solving Equation (28) at  $x = 150$  mm

It can be observed from Figure 4.2 that for the same input amplitude, we get different amplitude responses for different frequencies. Also, these values are increasing with frequency. Moreover, the solution is not dependent on time. At every time value, the same solution is obtained.

Figure 4.3 explores the theoretical solution discussed earlier to understand the effect of using different frequencies namely 3,6,12 and 24 kHz on the surface strain along the complete bar.

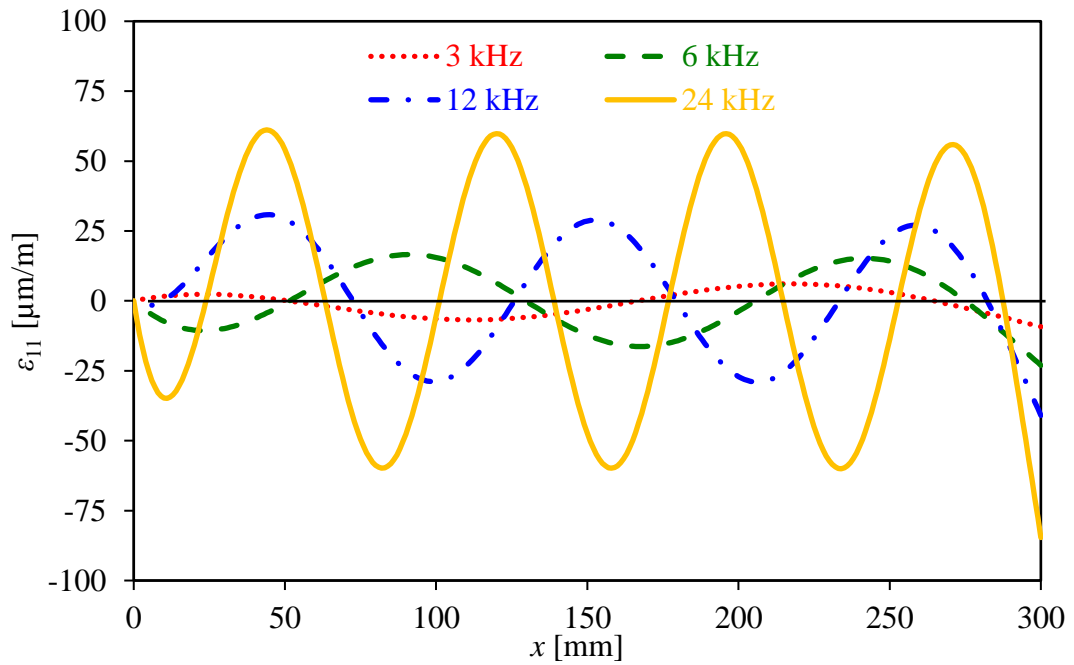


Figure 4.3: Surface strain along the bar using different frequencies

This analysis gives a good insight into the behavior of the bar when under the influence of external vibrations. It can be observed that increasing frequency increases the amplitude of the displacement. As the wavelength decreases with frequency, the number of zero nodes increases as well. Figure 4.4 shows the surface strain along the complete bar when under the effect of all the four frequencies combined.

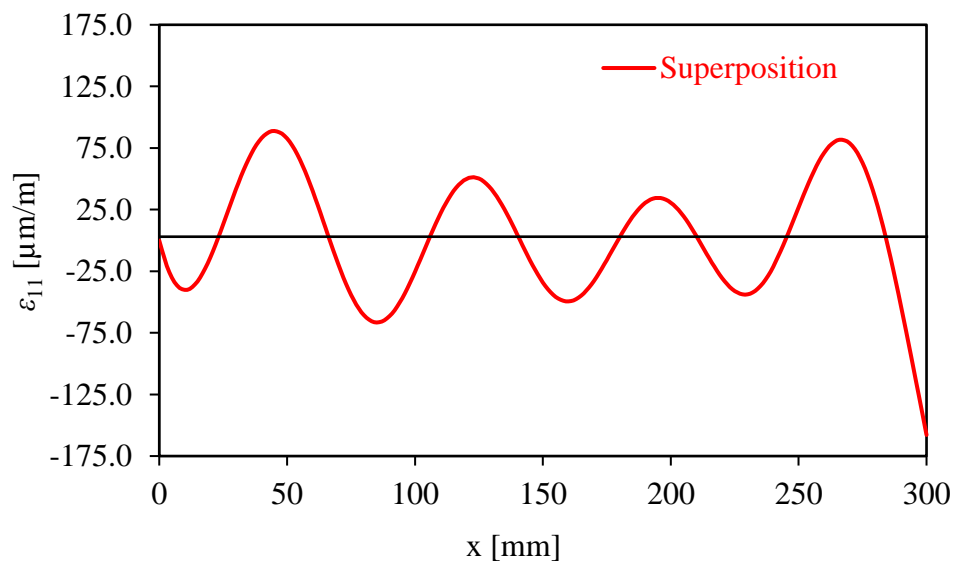


Figure 4.4: Surface strain along the bar using the combination of all frequencies

## Chapter 5. Modal and Harmonic Response Results

### 5.1. Fast Fourier Transform

To comprehensively understand the effect frequency has on the model, the results obtained from ABAQUS needs to be processed further. This can be done by performing a Fast Fourier Transform (FFT) on them. An FFT is an excellent tool used for processing signals. It is used to transform a signal from its elementary discipline to their frequency counterpart. The signal is sampled over a time period and is broken down into its various frequency components. The extracted components are sinusoidal waveforms of a single frequency, each with its own amplitude and phase.

**5.1.1. Short time Fourier transform.** The Short Time Fourier Transform (STFT) is a type of FFT which is used to detect the frequencies and phase from a part of the signal that is varying with time. Due to the nature of our analysis, performing an STFT is more beneficial than a standard FFT. In an STFT, the signal under analysis is essentially divided into smaller parts of equal time duration, then individual FFT is performed on each of them. An STFT can be done in two ways, the continuous-time STFT, and the discrete-time STFT.

In the continuous-time STFT, the signal to be processed is augmented with a window function. The new multiplied signal is processed by doing a Fourier Transform over the region where the window is passing until the whole signal is covered. This method is represented using Equation (42).

$$\text{STFT}\{x(t)\}(\tau, \omega) \equiv X(\tau, \omega) = \int_{-\infty}^{\infty} x(t)w(t - \tau)e^{-j\omega t} dt \quad (42)$$

where  $w(t)$  is the window function and  $x(t)$  is the signal under analysis.

In the discrete-time STFT, the signal to be processed is broken into frames. These frames should overlay each other to increase the accuracy of the results. Each of these frames is Fourier transformed, and the result is compiled together to get the STFT of the signal. Equation (43) denotes this process.

$$\text{STFT}\{x[n]\}(m, \omega) \equiv X(m, \omega) = \sum_{n=-\infty}^{\infty} x[n]w[n - m]e^{-j\omega n} \quad (43)$$

where  $w(n)$  is the window function and  $x(n)$  is the signal under analysis.

In this research, the discrete-time STFT method was used to analyze the sinusoidal frequencies. Figure 5.1 shows a strain output signal, obtained from a model analyzed in ABAQUS, that does not contain a crack or any other flaw. These signals are recorded at the middle of the bottom face of the bar i.e. at  $x = 150$  mm. The STFT is performed using MATLAB.

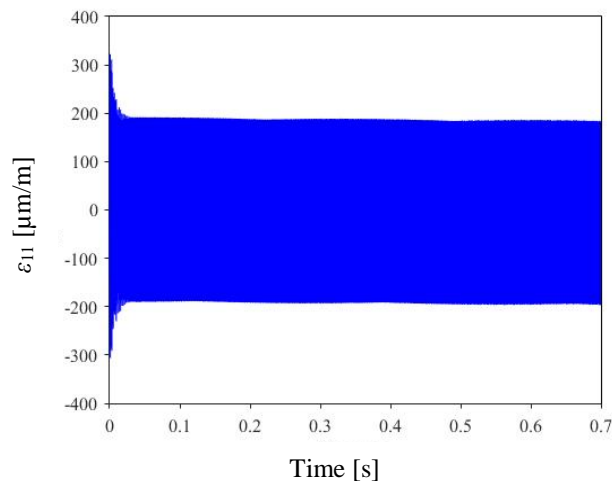


Figure 5.1: Finite element simulation of strain variation over the excitation period at  $x = 150$  mm and  $y = 7.5$  mm using a coarse mesh

The STFT performed on the plot in Figure 5.1 results in a spectrum of frequencies shown in Figure 5.2. This is a compilation of all the FFT's done over the complete time span. An individual FFT is shown in Figure 5.3.

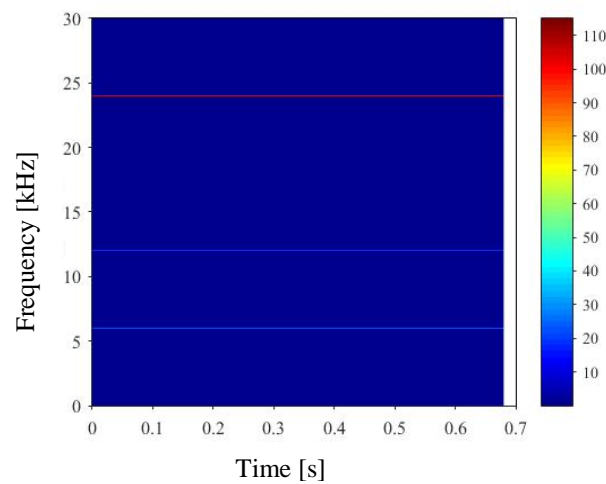


Figure 5.2: Spectrum of frequencies obtained upon performing STFT



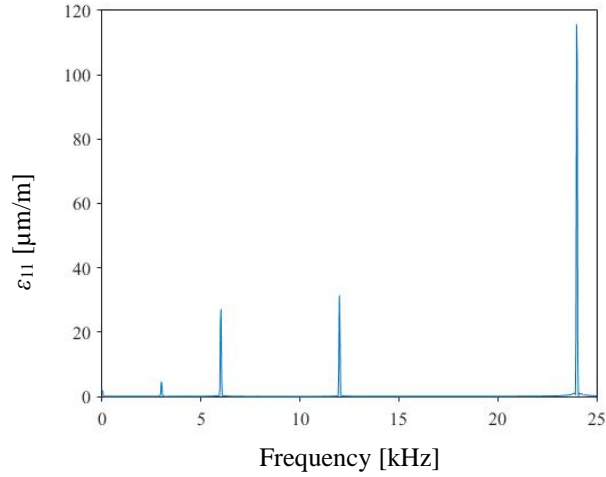


Figure 5.3: FFT taken from the spectrum at a single time value

**5.1.2. STFT time dependency.** Being a time-dependent analysis, it becomes essential to understand the effect time has on the STFT calculations. To do this the STFT is done at four random time values. The four-time values selected are 0.1802 s, 0.3604 s, 0.5407 s and 0.6717 s. These values are selected so that the whole time span of 0.7 sec is covered. Figure 5.4 shows the compiled STFT plot for a coarse mesh at the four-time values at  $x = 150$  mm.

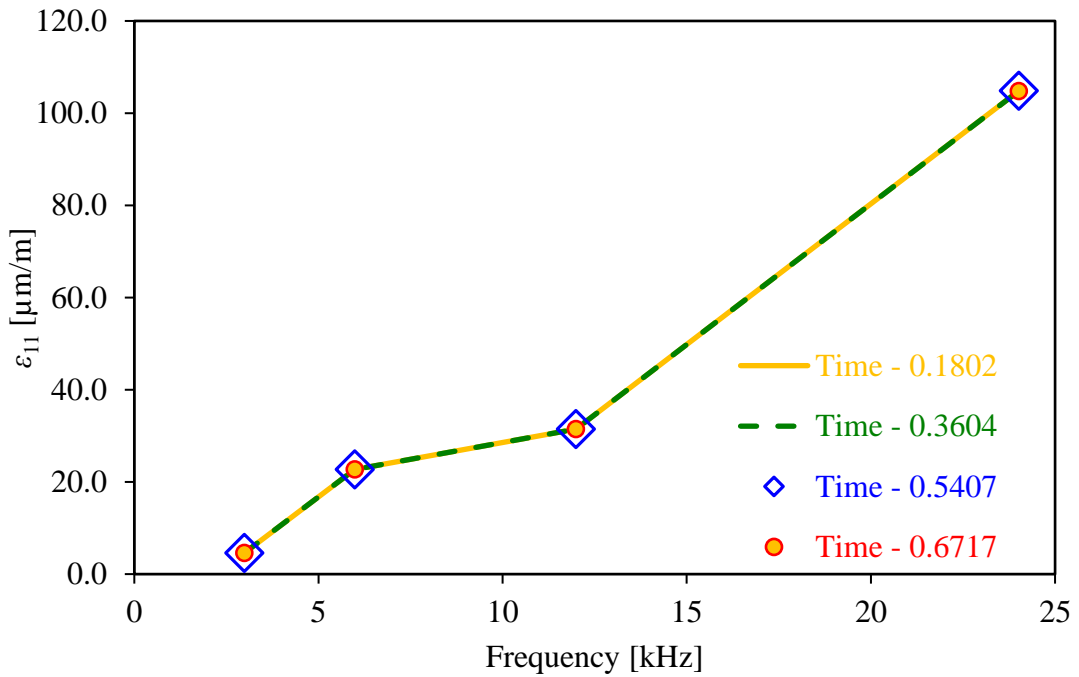


Figure 5.4: Frequency vs amplitude plot depicting the effect time has on the STFT

It can be concluded from Figure 5.4 that the STFT results are not affected by time. Thus, these values are not changing over the span of the analysis. This is in conformance with the theoretical solution shown in Figure 4.2. Hence, a single time value can be used to represent the complete analysis.

## 5.2. Modal and Harmonic Response Analysis

This section explores the behavior of the bar modelled in this research, upon introduction to vibrations. To do this, Firstly, modal analysis is performed in ABAQUS, which shows us the natural frequencies occurring in the bar. Then the bar is subjected to an explicit dynamic harmonic response analysis to understand its behavior and compare it to the theoretical model established in Chapter 4.

**5.2.1. Mechanical vibrations.** Before discussing the modal analysis, a brief insight into vibration is necessary. Vibration is usually of two types, free and forced vibration. Free vibration occurs when a system under observation is set into motion initially and warranted to further continue to vibrate. This system vibrates at its natural frequencies and comes to rest due to the presence of damping. However, forced vibration occurs when a mechanical system interacts with an external disturbance varying with time. In forced vibrations, the amplitude with which the system vibrates depends on the amplitude of the input disturbance as well as the harmonic response of the system. A mechanical system can be expressed using Equation (44).

$$[M]\{\ddot{x}\} + [C]\{\dot{x}\} + [K]\{x\} = \{F\} \quad (44)$$

where  $[M]$  is the mass matrix,  $[C]$  is the damping matrix,  $[K]$  is the stiffness matrix and  $\{F\}$  is the external force. If damping and external force is not present, Equation (44) reduces to Equation (45).

$$[M]\{\ddot{x}\} + [K]\{x\} = 0 \quad (45)$$

Assuming  $[M]^{-1}[K] = [B]$ , we get

$$\{\ddot{x}\} + [B]\{x\} = 0 \quad (46)$$

Equation (46) is a differential equation whose solution results in providing eigenvalues of the system. These eigenvalues are the natural frequencies with which

the system vibrates. Every mechanical system has an unlimited number of natural frequencies. ABAQUS can be used to calculate these.

**5.2.2. Modal analysis.** A modal analysis was performed using ABAQUS to calculate the natural frequencies of a 300 mm × 15 mm × 15 mm bar. The considered model does not contain a crack or any other flaw. Modal analysis was done between 0 and 25000 Hz in order to consider all the needed frequencies. All the data from the analysis, the modal frequencies and mode shape were observed. The used model is shown in Figure 5.5. The first natural frequency was found to be 136.07 Hz. Table 5.1 shows a few of the other modal frequencies.



Figure 5.5: Model created in ABAQUS for performing the modal analysis

Table 5.1: Modal frequencies for the model illustrated in Figure (5.5)

Mode	Frequency [Hz]	Mode	Frequency [Hz]
1	136.7	16	11958
3	842.97	18	13840
5	2318.8	21	17729
9	4433.9	25	21885

**5.2.3. Explicit harmonic response.** To corroborate the results obtained from the theoretical solution, an explicit dynamic harmonic response was performed on the model. The model under analysis does not contain any defects in it. The main purpose of this analysis was to observe the response the bar has under the applied boundary and loading conditions. These conditions have been discussed in Section 3.9. Four different meshes were used, namely the coarse, normal, fine and very fine. All the named meshes have been discussed in detail in Table 3.4. Due to the absence of a crack, only the cube type mesh was taken into consideration.

An STFT was performed on the strain output obtained from the analysis similar to Section 5.1. This strain output was recorded from the elements situated in the bottom of the bar. Figure 5.6 shows the position of an assumed strain gauge for the coarse mesh. It can be seen from Figure 5.6 that the strain gauge elements are at the middle of the bottom face of the bar. Since we have four different types of mesh, each case will have a different number of strain gauge elements. Table 5.2 shows the number of elements present in each case

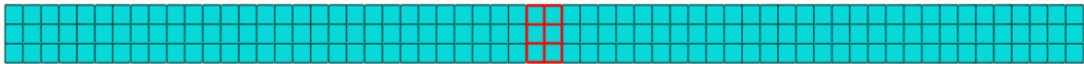


Figure 5.6: Assumed strain gauge position at the bottom of the bar

Table 5.2: Number of strain gauge elements for different meshes

Mesh	No. of elements
Coarse	6
Normal	8
Fine	12
Very Fine	30

The strain output at the middle nodes was calculated by averaging the elements encompassing that node. Figure 5.7 shows the plot containing the various STFT calculated for the different mesh sizes. The theoretical solution obtained in Chapter 4 is also added in the figure for comparison. The strain input for the STFT is

obtained by averaging all the nodes along the crack. This will ensure that the solution obtained is exactly at  $x = 150$  mm.

Figure 5.7 provides substantial proof that the mesh size has an enormous effect on the simulation of wave propagation. It can be seen from the plot that for lower frequencies, even coarser mesh results in convergence, but as the frequency increases, a finer mesh is required to achieve accurate solutions. Also, at 24 kHz, the convergence in result occurred using the fine mesh. Furthermore, the theoretical solution is in close accordance with the results obtained from the fine and very fine mesh.

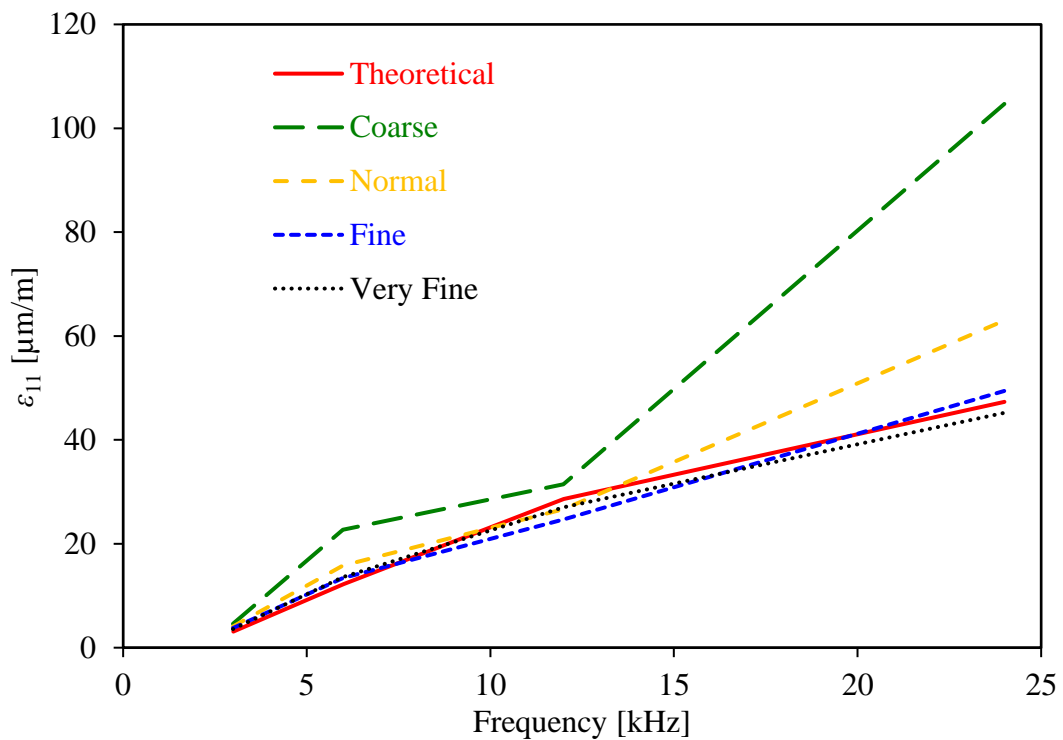


Figure 5.7: Frequency vs amplitude plot comparing the harmonic response for various mesh sizes

## Chapter 6. Heat Generation Results

### 6.1. Heat Generation Analysis

Based on all the model parameters defined and discussed in previous sections, a heat generation analysis was done on the bar. The analysis was done on the five crack sizes discussed in Section 3.2. The temperature over the crack was plotted by averaging the nodes accommodated by the crack on the top surface of the bar. Figure 6.1 shows these nodes in one of the cases analyzed. Initially, the 5 mm crack was analyzed with all the three types of mesh. These results are shown in Figure 6.2 (a – f). For the remaining crack sizes, only the circular mesh was used. Figure 6.3 shows the heat generation results for crack sizes 2 mm, 3 mm, 4 mm, 5 mm, and 6 mm respectively.

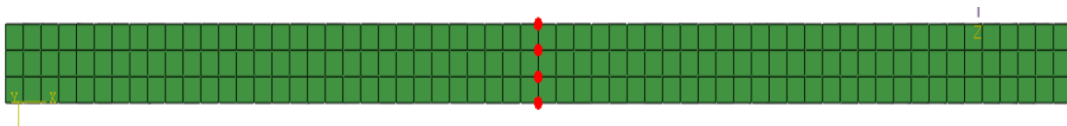


Figure 6.1 shows the nodes considered for calculating the average temperature over the crack

Figure 6.2 (a, c and e) shows the variation the mesh has on the heat generation for a 5 mm crack. It can be seen for the rectangular and circular meshes that the heat generated over the crack decreases as the bar is finely meshed. But for the semi-circular mesh, the heat generation is unresponsive to the element size. For any element size, the temperature profile for the semi-circular mesh does not change that much.

Figure 6.2 (b, d, and f) shows the effect the element size has on the heat generation. For the three types of meshing discussed in Section 3.8, the coarse, normal and fine mesh were plotted. It can be observed that for the coarse and normal mesh, the temperature plots are erratic, and no relation between them can be observed. But for the fine mesh, the heat generation plots are in close vicinity to each other and shows a convergence irrespective of the mesh type. This is in accordance with the results of the harmonic response analysis discussed in Section 5.2.4. Since for the 24

kHz frequency we were getting convergence at the usage of a fine mesh, the temperature analysis also indicates a similar behavior.

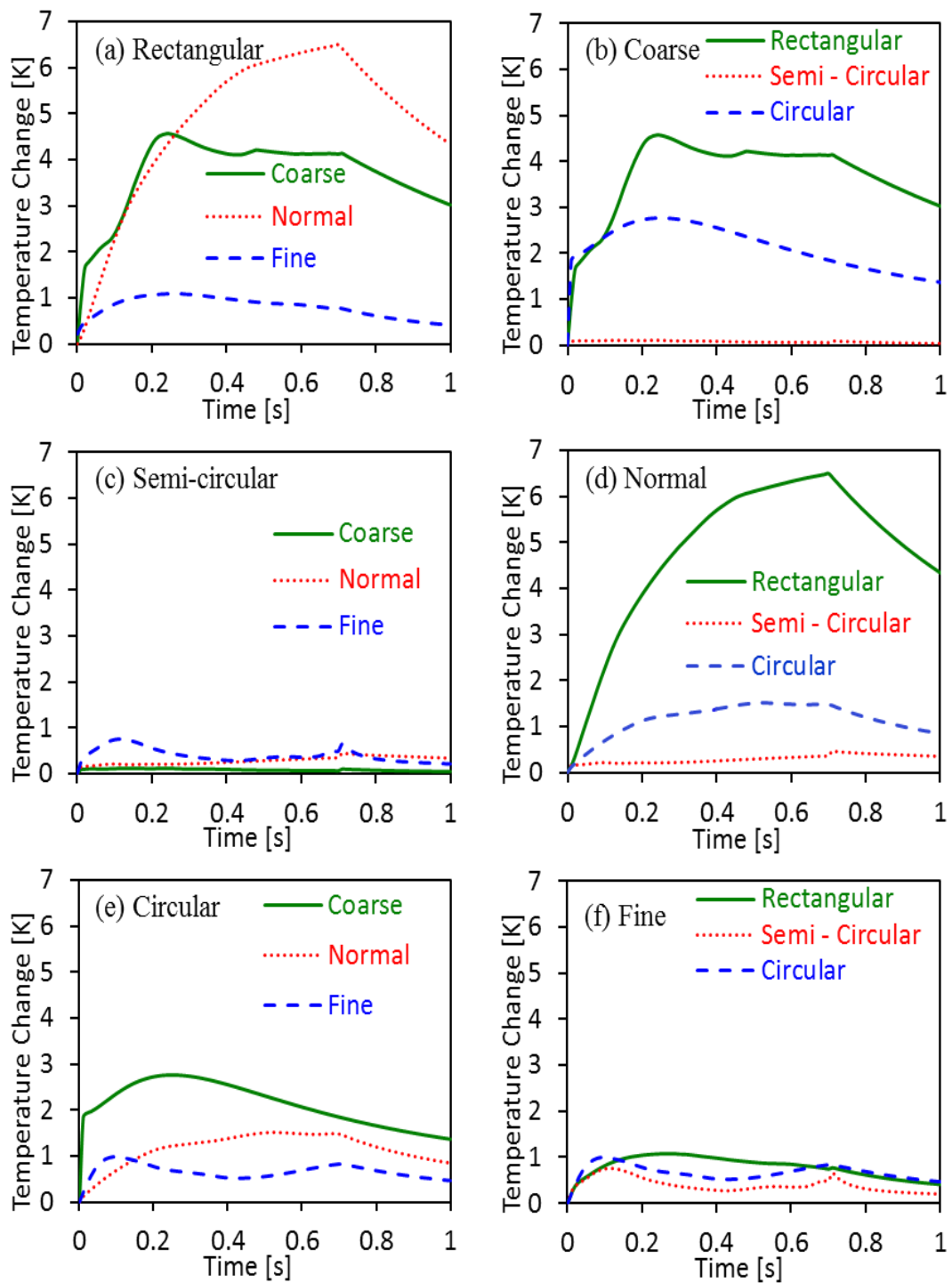


Figure 6.2: Temperature variation with time using different mesh criteria for the 5 mm crack

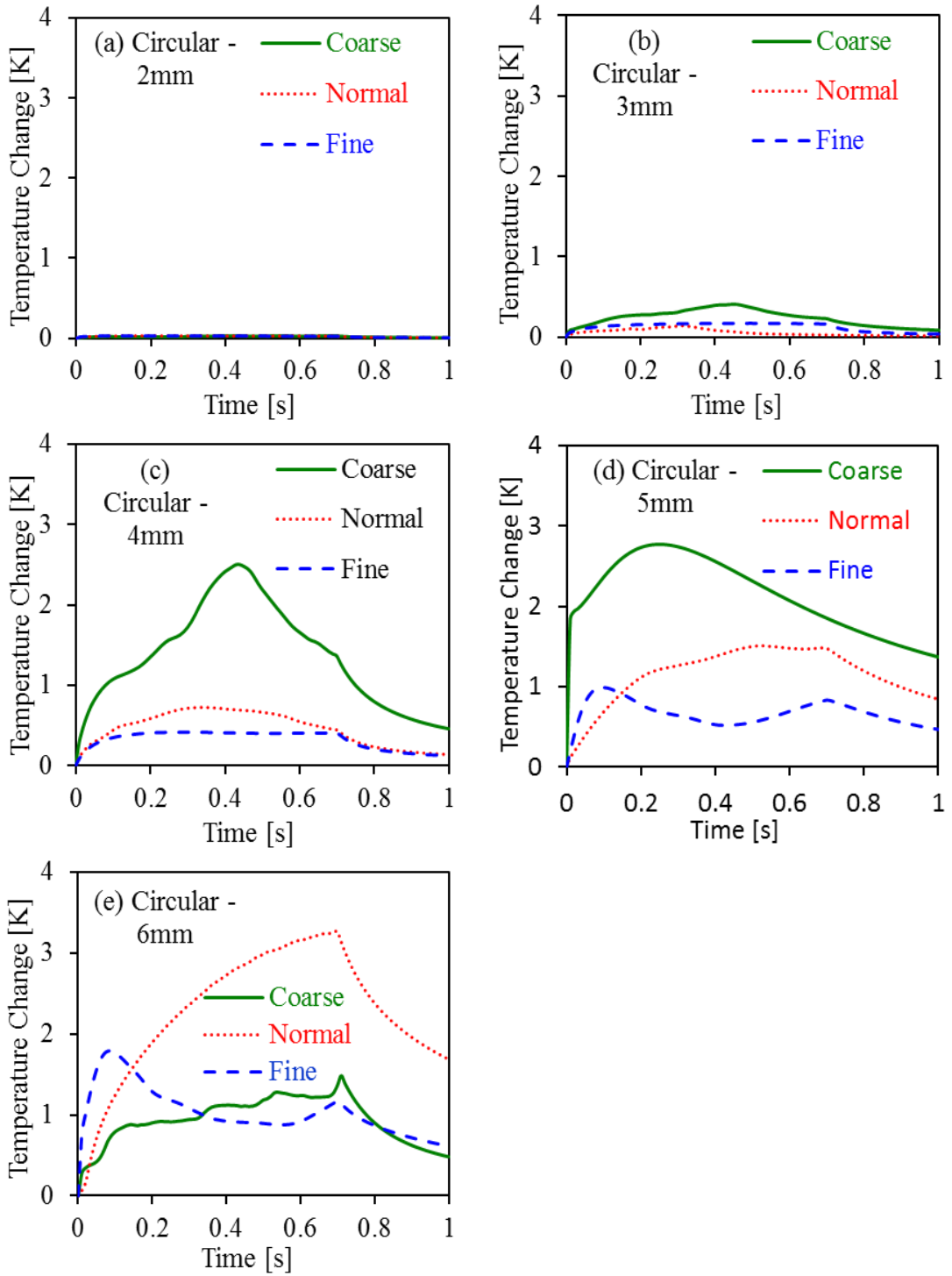


Figure 6.3: Time vs temperature plots: (a) 2 mm, (b) 3 mm, (c) 4 mm, (d) 5 mm and (e) 6 mm cracks simulated using circular mesh criteria



## 6.2. Temperature Maps

The current section shows the temperature maps generated in ABAQUS for the various crack sizes modelled. The top and front views of the 5 mm crack model are shown in Figure 6.4, 6.5 and 6.6. The temperature maps plotted are at  $t = 0.7$  s.

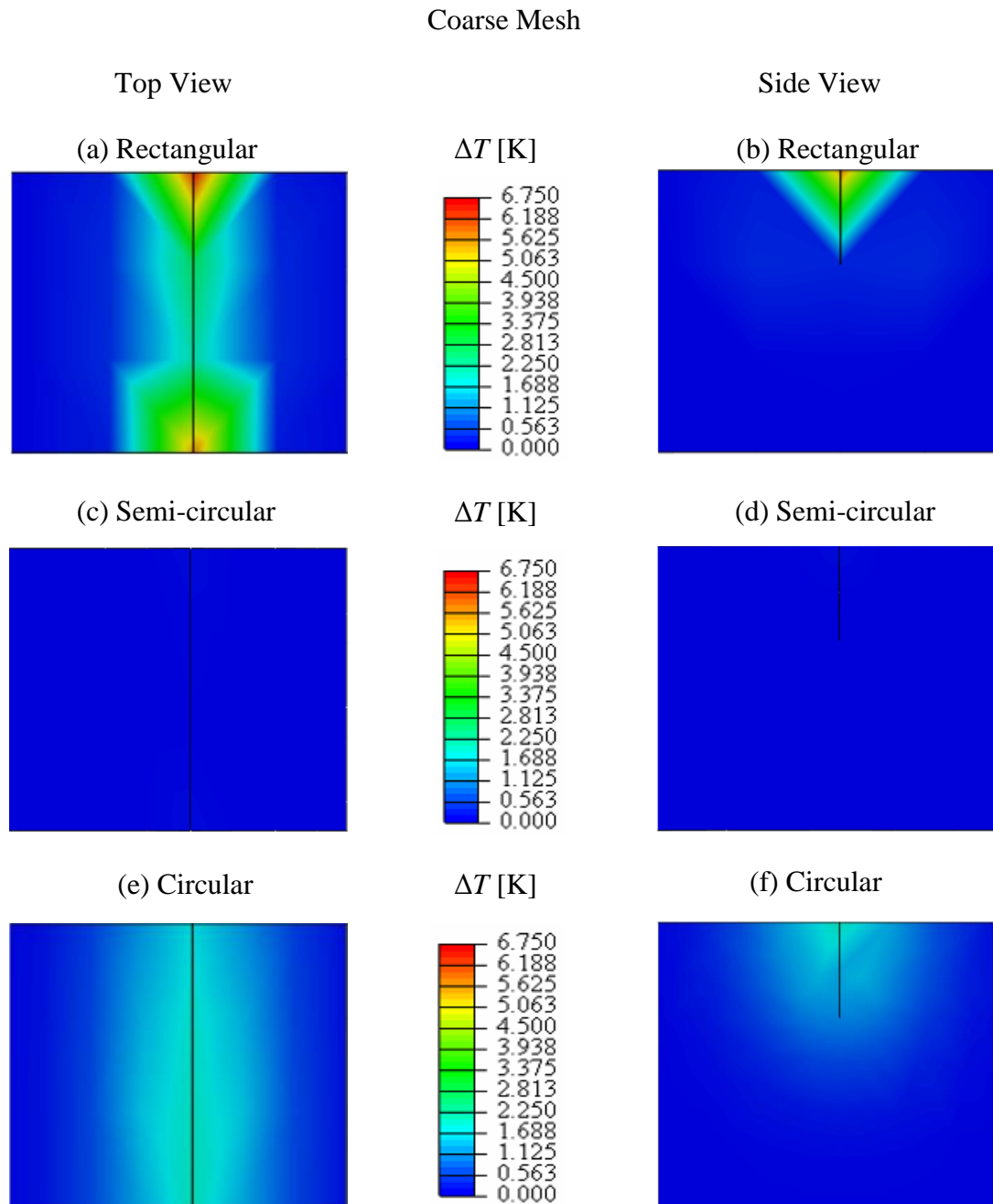


Figure 6.4: Temperature maps for the 5 mm crack using different coarse mesh types at 0.7 s

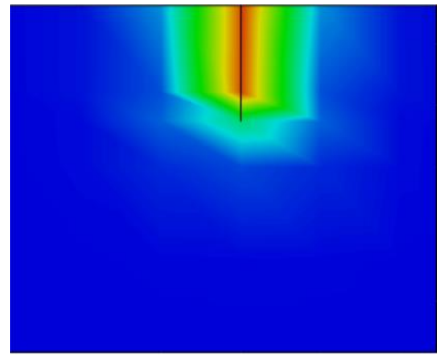
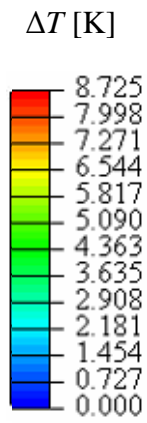
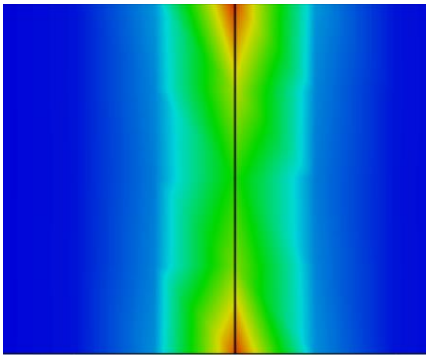
Normal Mesh

Top View

Side View

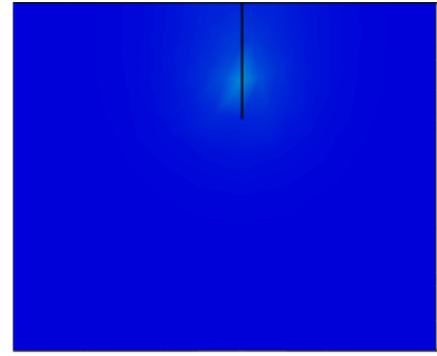
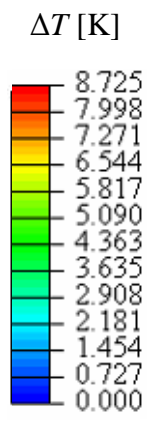
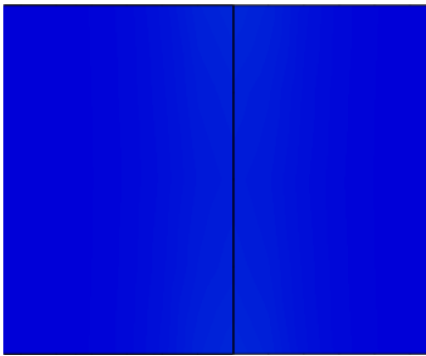
(a) Rectangular

(b) Rectangular



(c) Semi-circular

(d) Semi-circular



(e) Circular

(f) Circular

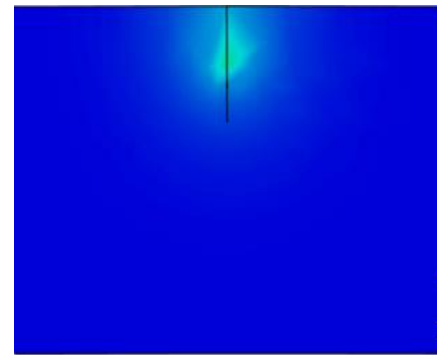
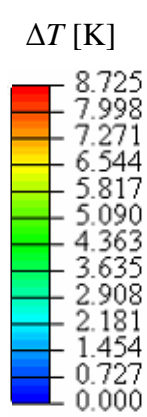
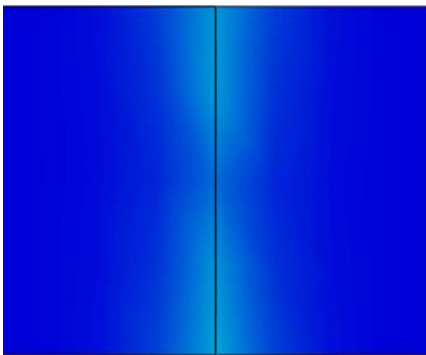


Figure 6.5: Temperature maps for the 5 mm crack using different normal mesh types at 0.7 s

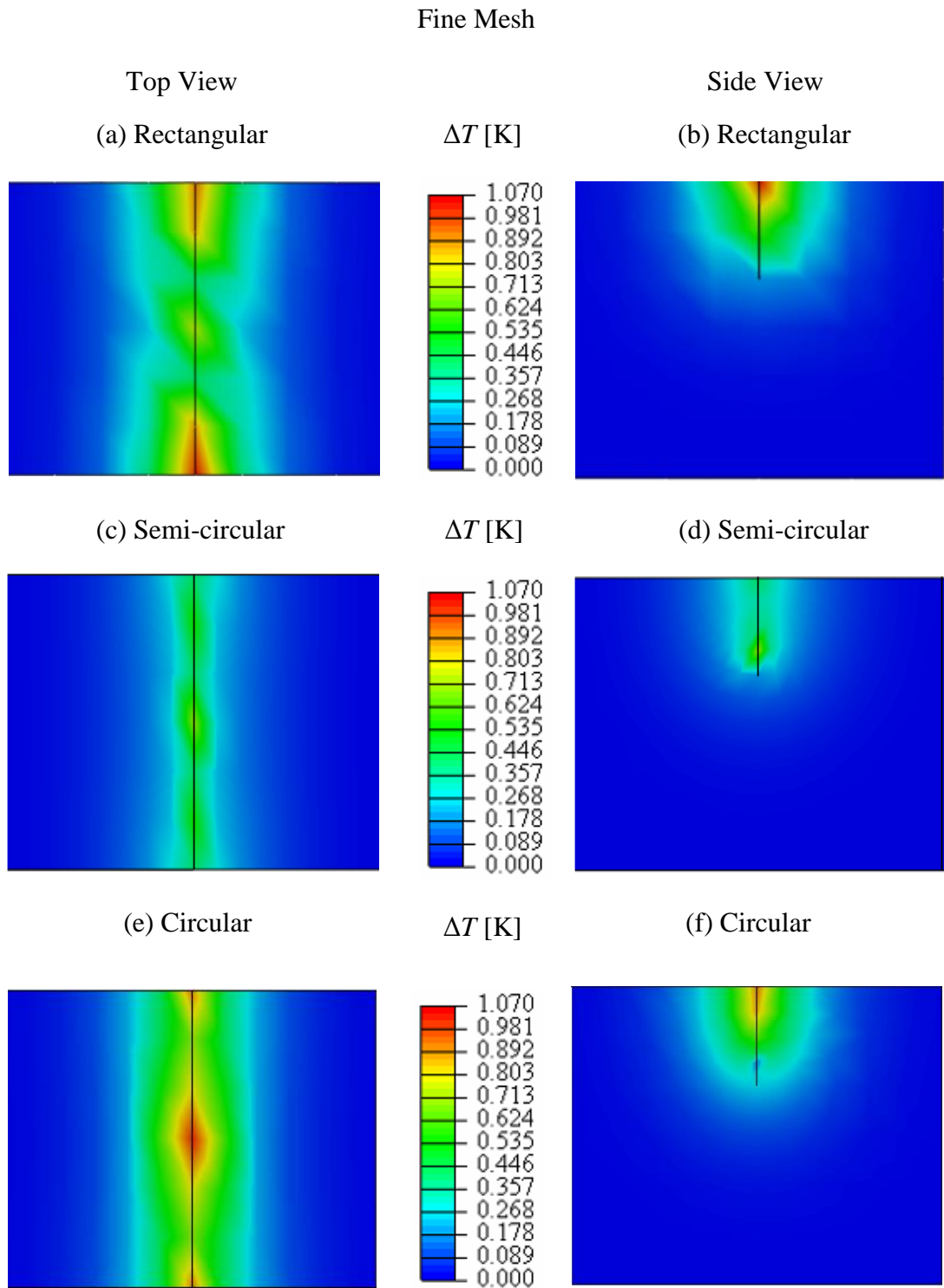


Figure 6.6: Temperature maps for the 5 mm crack using different fine mesh types at 0.7 s

The temperature maps gave a good insight into the way heat is generated and propagated around the crack. It can be clearly seen from Figure 6.4, 6.5 and 6.6 that as the mesh is refined, we get symmetrical heat profile.

### 6.3. Hybrid case

As it was seen in Section 6.2, a fine mesh is required for converging heat generation results. But as witnessed in Section 3.6, the stable time increment is a factor of the element size. Hence as element size reduces, the stable time increment reduces as well. Thus, increasing the computational time for our analysis. Having large computational time is not favorable as the analysis may take days to complete. Thus, this section attempts to counter this problem. To decrease the computational time a model was created such that it contained a fine mesh near the crack region which transitioned to a coarse mesh towards the end of the bar. Figure 6.7 shows the model. The results of the analysis can be seen in Figure 6.8.

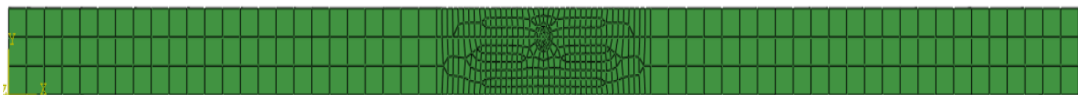


Figure 6.7: A case of hybrid mesh in which the bar transitions from a coarse to a fine mesh in the middle around the crack

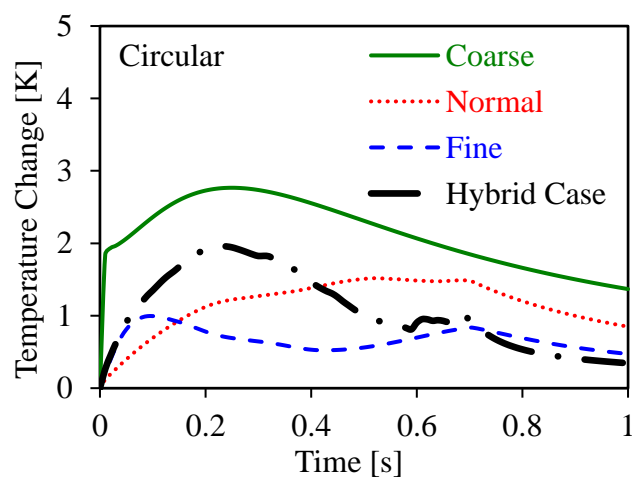


Figure 6.8: Time vs temperature plot exhibiting the effect of different criteria of circular meshes

The model contained a 5 mm crack and the circular mesh was used to capture the generated heat. The model had all the parameters defined as discussed in the previous sections.

It can be concluded from Figure 6.8 that a hybrid mesh results in a solution in between the coarse and the fine case. Thus, using a coarser mesh on the outside and a finer mesh near the crack does not result in an accurate solution. Also Figure 6.9 shows the temperature maps of the top and side views of the hybrid case.

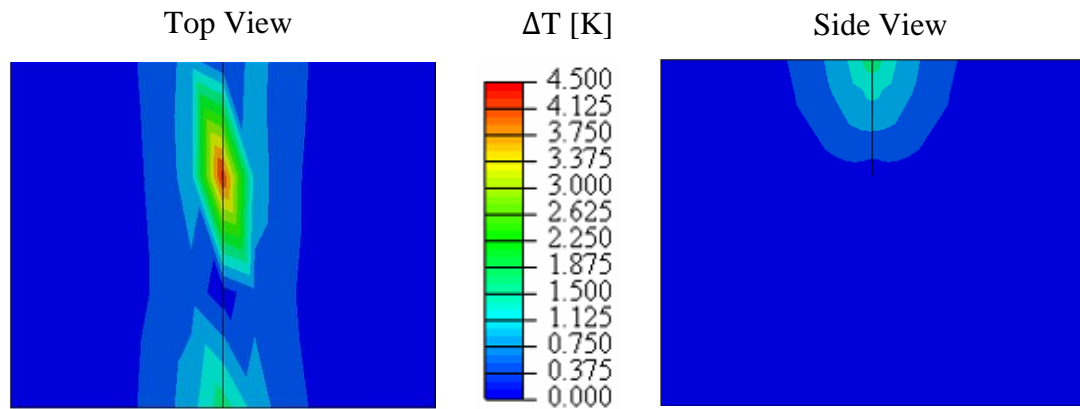


Figure 6.9: Temperature maps for 5 mm crack using hybrid mesh at 0.7 s: (a) top view and (b) side view

Thus, irrespective of the mesh type used, if the element size is kept fine enough, we would see a convergence in the results. Therefore, the higher the frequency with which the system is vibrated, the smaller the element size required to capture the correct heat generation. Furthermore, this element size is needed to be maintained all over the bar. If part of the bar is meshed with a coarser mesh than the other, the observed results would be inaccurate and unreliable to predict the actual nature of the bar under those conditions.

#### 6.4. Validating the Model

To validate the accuracy of the results established in this thesis, a concrete model creation in ABAQUS was necessary. To achieve this, a model similar to that used by Morbidini and Cawley was developed [24]. A vibrothermographic model was established based on experimental analysis of the same. The key difference between the model used in this research and their work is the presence of chaotic vibrations.

Since the work done by Morbidini and Cawley [24] uses an experimental setup, chaotic vibrations were present due to the interaction of a physical transducer with the specimen. The model established in this work uses a single frequency, whose amplitude is fixed to achieve a similar temperature profile as substantiated in the work done by Morbidini and Cawley [24].

A bar of  $300\text{ mm} \times 19\text{ mm} \times 17\text{ mm}$  was made in ABAQUS. A 1.4 mm crack was introduced in the center similar to the way discussed in Section 3.2. The meshed model is shown in Figure 6.10.

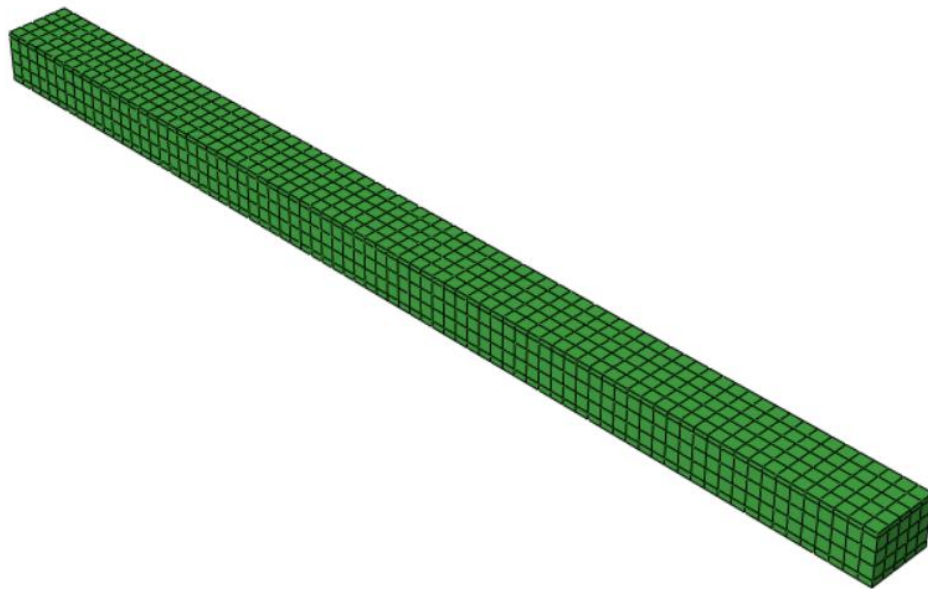


Figure 6.10: Bar containing a 1.4 mm crack, used for validating the models designed in ABAQUS

To simulate the experimental setup without the clamp and the transducer, the left side of the bar was fixed in all degree of freedoms and a displacement load of  $11\mu\text{m}$  is applied in a rectangular area on the top surface in the downward direction. A complete overview of these boundary conditions can be seen in Figure 6.11 (a). Figure 6.11 (b) shows the fixed left end and Figure 6.11 (c) shows the right side of the top surface.

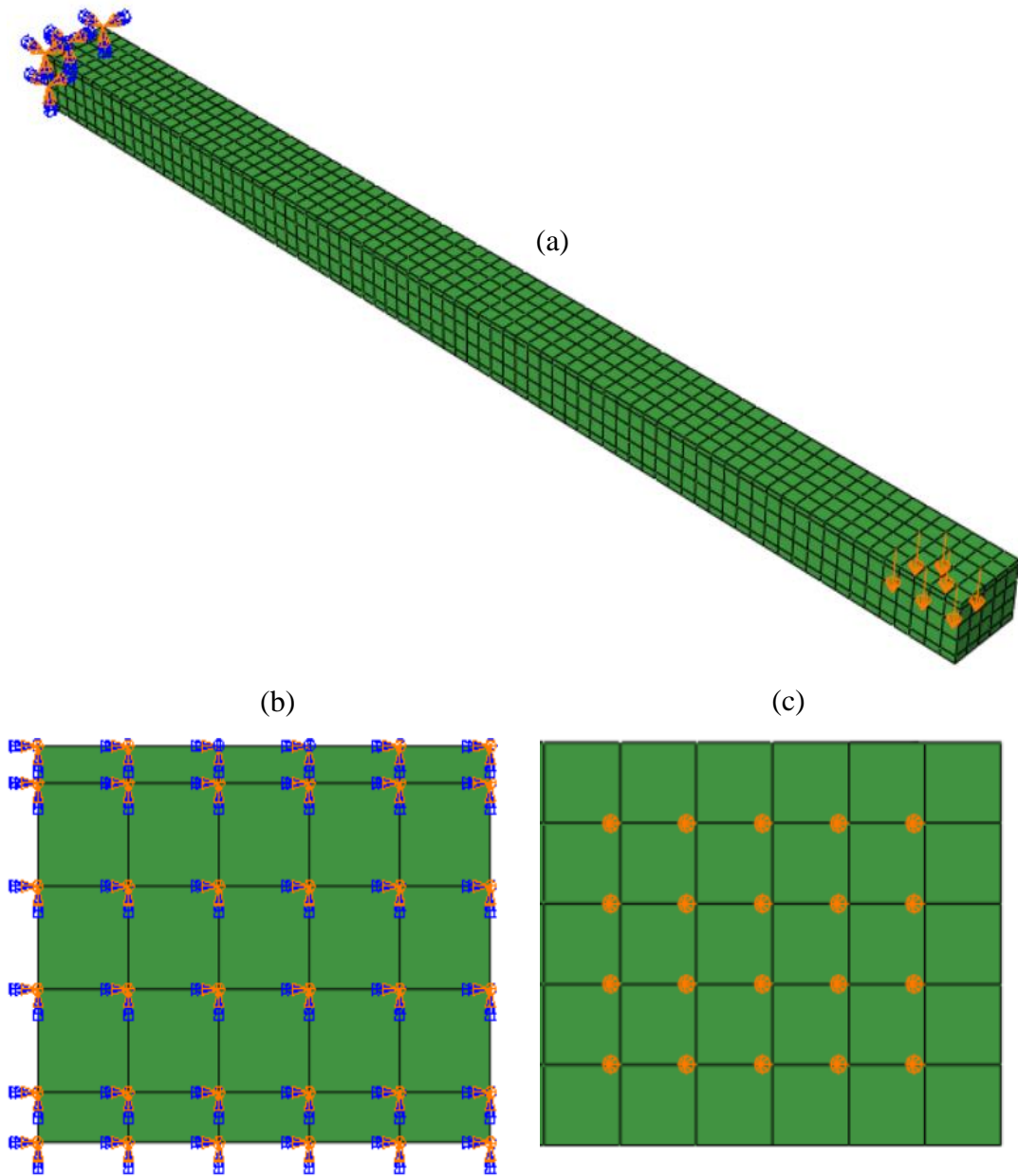


Figure 6.11: Load and boundary conditions applied on the bar depicted in Figure (6.10), part (a) overview of the bar with the applied boundary conditions, part (b) fixed left side end and part (c) displacement load applied on the top right surface

The temperature map at the crack surface is shown in Figure 6.12 and 6.13. Figure 6.12 shows the crack from the top, while Figure 6.13 shows the crack from the front. This map will become sharper and more symmetric with a finer mesh. Furthermore, Figure 6.14 shows the temperature versus time plot. The time span for the analysis is 2.5 sec.

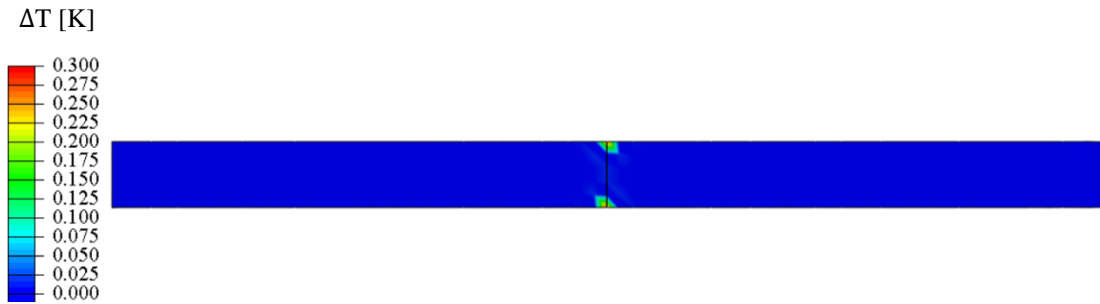


Figure 6.12: Temperature map as seen from the top, for the model shown in Figure (6.10 and 6.11)



Figure 6.13: Temperature map as seen from the side, for the model shown in Figure (6.10 and 6.11)

It can be seen from Figure 6.14 that the temperature plot is very similar to the work done by M. Morbidini [24]. For similar bar and crack sizes, it can be concluded that the model behavior is comparable, and hence can be used as a framework for analyzing different models as required in this research.

## 6.5. Heating Index

To increase the consistency of vibrothermography, M. Morbidini and P. Cawley [24] developed a calibration process. The term heating index was introduced, which is directly related to the calculated temperature rise. Based on the calibration procedure, a threshold value of the heating index can be calculated for any model. Thus, to increase the probability of detection of the crack, the heat generation over the crack must be more than the threshold heating index.

The temperature rise at the crack is directly proportional to the power dissipated over it, which is defined by Equation (47).



$$P = 2\pi \sum_n \eta_{crack,n} f_n V_n \quad (47)$$

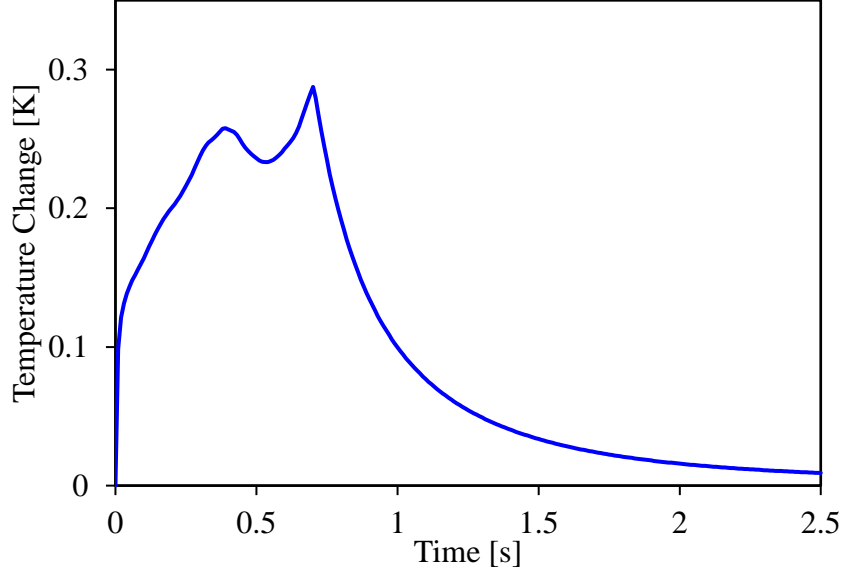


Figure 6.14: Time vs temperature plot for the model illustrated in Figure (6.10)

where  $P$  is the dissipated power,  $\eta_{crack,n}$  is the crack loss factor in mode  $n$ ,  $f_n$  is the vibrational frequency at mode  $n$  and  $V_n$  is the modal strain energy. It can be seen from Equation (47) that the dissipated power over the crack is dependent on  $\eta_{crack}$ ,  $f$  and  $V$  at every mode. Since the modal strain energy is proportional to the square of vibrational strain, it can be replaced by  $\varepsilon^2$ . Furthermore, for a constant size crack, the vibrational frequency can be related to  $f$  and  $V$  only.

Since the variables for dissipated power have been altered, a new variable energy index can be defined using Equation (48).

$$EI = \sum_n W_n \varepsilon_n^2 \quad (48)$$

where  $W_n = \frac{f_n}{f_0}$  is the weighted proportion of the frequency at the  $n^{\text{th}}$  mode to the reference central frequency. Since energy index cannot express the heat generated over a crack, a heating index is used to capture this. Equation (49) defines the heating index as:

$$HI(\tau) = \int_0^\tau e^{k(t-\tau)} EI(t) dt \quad (49)$$

where  $\tau$  is the time,  $t$  is integration time variable and  $k$  is a constant. In this research, the heating index has been calculated for all the cases considered. The process used is in accordance with the work done by Morbidini and Cawley [24]. Figure 6.15 shows an example of the procedure discussed in this section. The strain is obtained from ABAQUS. The energy index is calculated using MATLAB to estimate the heating index.

Figure 6.16 plots the heating index for different types of meshes for a 5 mm crack. While Figure 6.17 plots the heating index for different crack sizes for a circular fine mesh. It can be seen from Figure 6.17 that heating index is directly affected by the crack size. As the crack size increases, the heating index increases as well. Moreover Figure 6.16 shows the effect of different mesh type on the heating index. For the 5 mm crack, the highest value of the heating index was obtained from the circular mesh.

Since a higher heating index increases the probability of detection of the crack, it can be concluded that the larger the crack size, its chances of detection increase. Furthermore, the circular mesh is the most efficient mesh during a heating analysis of a crack using the finite element method, since it results in the highest heating index.

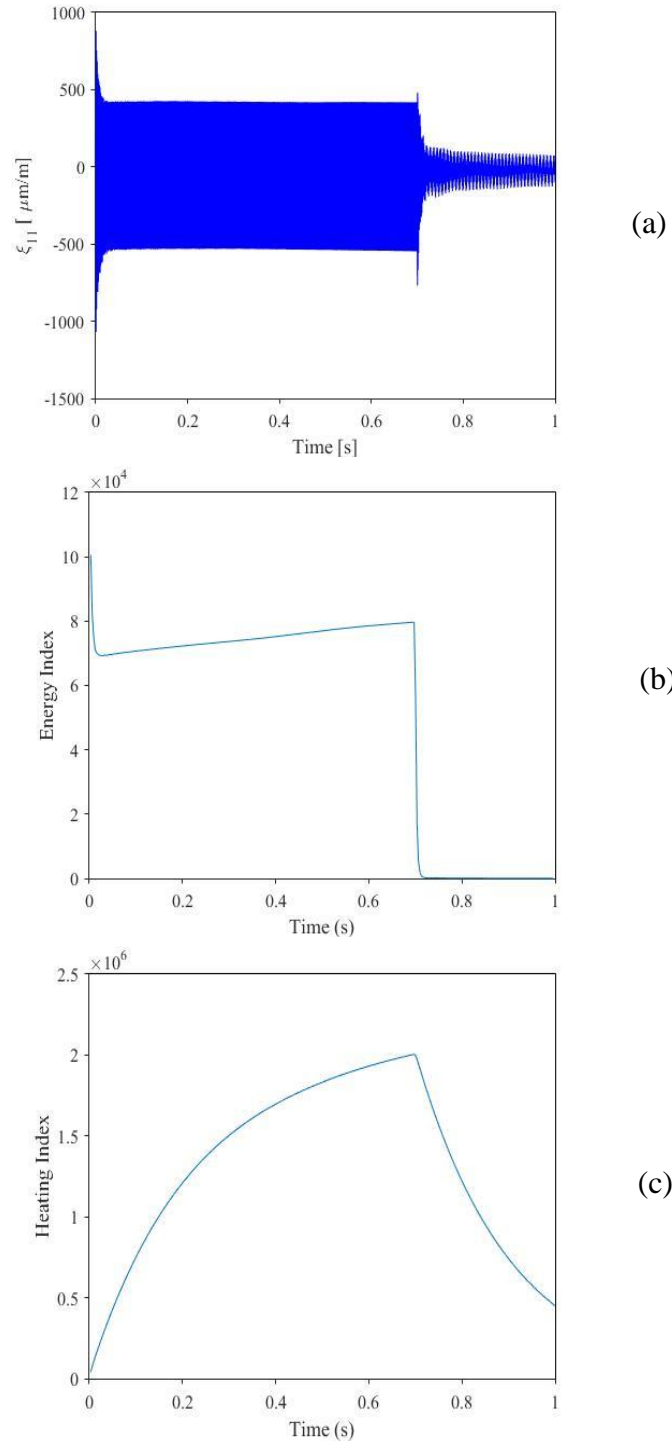


Figure 6.15: An example showing the process of calculation of heating index, (a) the strain output from ABAQUS, (b) energy index vs time and (c) heating index vs time

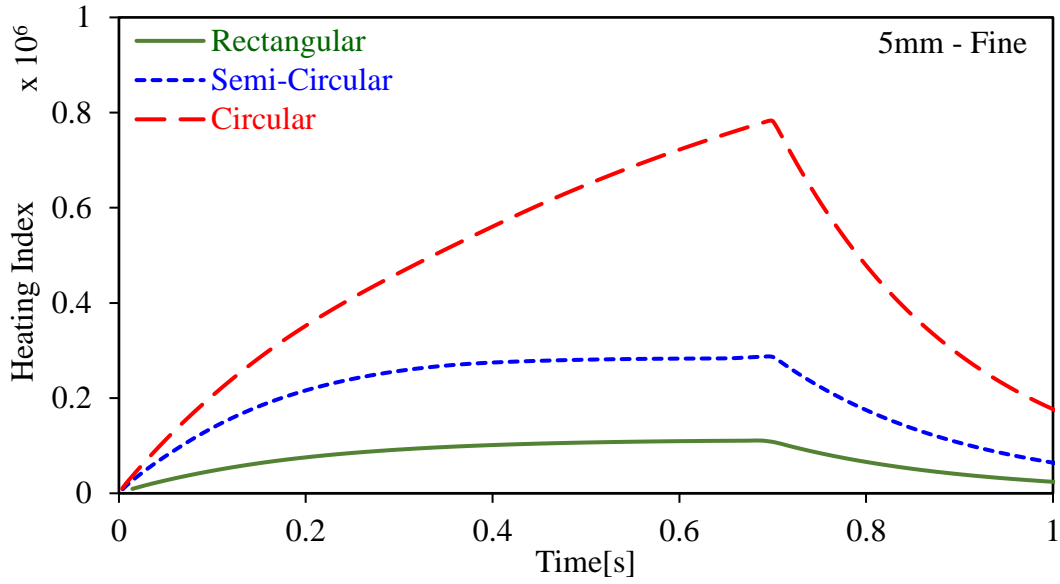


Figure 6.16: Time vs heating index plot for a 5 mm crack comparing different types of fine mesh

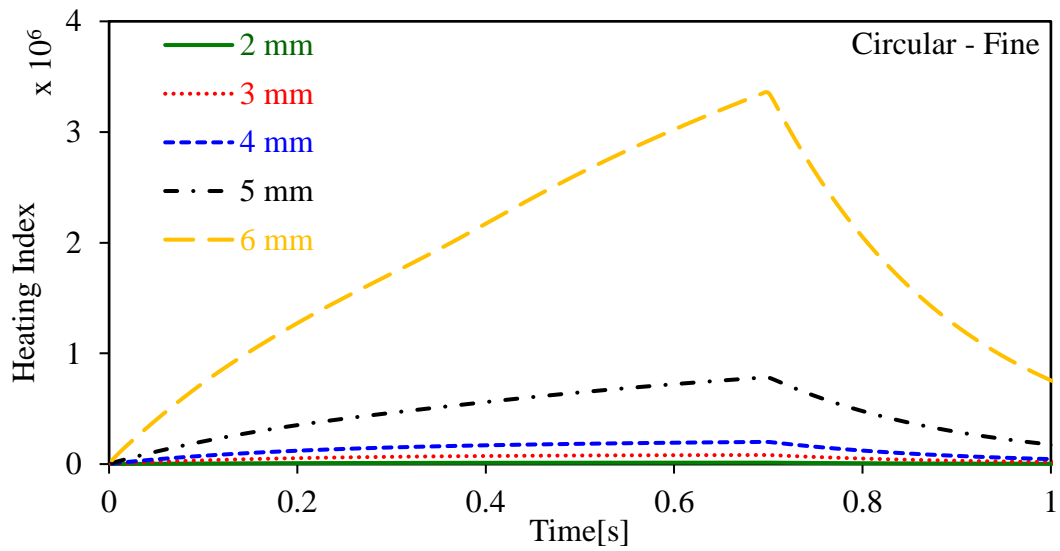


Figure 6.17: Time vs heating index plot for circular fine mesh comparing different crack sizes

## Chapter 7. Conclusion and Future Work

Nondestructive evaluation techniques for defect detection are extremely necessary for any industry to work efficiently. Thus, developing new and reliable techniques is not a question of doubt. Vibrothermography is one such upcoming technique which shows promising potential. It is a fast and reliable technique used for detecting a wide range of defects. However, the multidisciplinary nature of this technique makes it rather difficult to theoretically capture the system response without the proper application of finite element methods. In recent years, the field of vibrothermography has been explored using the finite element method. But the results so far have provided a partial picture of the process.

The work done in this thesis has highlighted this problem and approached this obstacle exclusively by establishing a theoretical model that embraces the basic vibrothermography process. Based on this, a finite element software package has been used to accurately model the heat generation process involved in vibrothermography. The complete process involved, from defining the model to the heat generation results, has been discussed in detail. This model is utilized to assess the convergence of FE dynamic system response that helps in determining the maximum element size needed for realistic elastic wave propagation throughout the sample. This is done by comparing the dynamic strain response from ABAQUS for different frequencies for particular sized elements. Furthermore, when higher frequencies are involved in the analysis, a finer mesh is required as compared to lower frequencies. For the case of 24 kHz, the convergence was achieved when the mesh element size was kept 2.5 mm throughout the model. Moreover, it was also established that the whole model needs to be meshed with elements of similar size.

For the defined model, the most important aspect was found to be the mesh used during the process. It was established that both the element size and the type of mesh used around the crack region are influential not only on the amount, but also on the demeanor of the induced heat. Moreover, the association of a crack has an added disadvantage of a singularity at the crack tip. Hence to avoid this, the mesh is required to be modified at the crack tip. Three types of mesh were assessed, namely rectangular, semi-circular and circular to properly capture the singularity at the crack tip. Out of the three mesh type used, the circular mesh proved to be the most effective

in capturing the thermal aspects of vibrothermography. Furthermore, it was also found to be converging to the singular quarter-node element solution. The temperature maps also provide a good understanding of how different types of mesh generate heat.

The effect crack size has on the heat generation was also investigated. For the different crack sizes used, it can be clearly seen that as the crack size increases, so does the heat generated over it. This is also established from the calculation of the heating index. The heating index plots also point out the advantage a circular mesh has on the other types.

This thesis has aimed to establish the minimum requirements needed to accurately model vibrothermography. Any deviation from the optimized mesh criteria and element size, i.e., selecting larger element sizes, will adversely affect the relative motion of crack surfaces and frictional heat generation. The results from FEM have been juxtaposed with the results from the theoretical model and are found to be similar. This has not only increased the understanding of the process of vibrothermography but has also brought it a step closer to be accepted commercially. With this simple established model, future work will involve working on a model with acoustic chaos. The effect of crack orientation on heat generation can also be studied.

## References

- [1] K. L. Reifsnider, E. G. Henneke, and W. W. Stinchcomb, "The mechanics of vibrothermography," in *Mechanics of Nondestructive Testing*, New York: Plenum Press, 1980, pp. 249-276
- [2] J. Renshaw, S. D. Holland, R. B. Thompson, and J. Anderegg, "Vibration-induced tribological damage to fracture surfaces via vibrothermography," *Int. J. Fatigue*, vol. 33, no. 7, pp. 849-857, July 2011.
- [3] S. D. Holland, C. Uhl, Z. Ouyang, T. Bantel, M. Li, W. Q. Meeker, J. Lively, L. Brasche, and D. Eisenmann, "Quantifying the vibrothermographic effect," *NDT & E Int.*, vol. 44, no. 8, pp. 775-782, December 2011.
- [4] F. Mabrouki, M. Thomas, M. Genest, and A. Fahr, "Frictional heating model for efficient use of vibrothermography," *NDT & E Int.*, vol. 42, no. 5, pp. 345-352, July 2009.
- [5] J. Renshaw, J. C. Chen, S. D. Holland, and R. B. Thompson, "The sources of heat generation in vibrothermography," *NDT & E Int.*, vol. 44, no. 8, pp. 736-739, December 2011.
- [6] J. Renshaw, S. D. Holland, and D. J. Barnard, "Viscous material-filled synthetic defects for vibrothermography," *NDT & E Int.*, vol. 42, no. 8, pp. 753-756, December 2009.
- [7] R. Montanini and F. Freni, "Correlation between vibrational mode shapes and viscoelastic heat generation in vibrothermography," *NDT & E Int.*, vol. 58, pp. 43-48, September 2013.
- [8] F. Mabrouki, M. Thomas, M. Genest, and A. Fahr, "Numerical modeling of vibrothermography based on plastic deformation," *NDT & E Int.*, vol. 43, no. 6, pp. 476-483, September 2010.
- [9] M. Rothenfusser and C. Homma, "Acoustic thermography: vibrational modes of cracks and the mechanism of heat generation," in *Proc. AIP*, 2005, pp. 624-631.
- [10] J. Renshaw and S. D. Holland, "Full-field vibration measurement for vibrothermography," in *Proc. AIP*, 2008, pp. 498-503.
- [11] H. Xiaoyan, Z. Zeng, W. Li, M. S. Islam, J. Lu, V. Loggins, E. Yitamben, L. D. Favro, G. Newaz, and R. L. Thomas, "Acoustic chaos for enhanced detectability of cracks by sonic infrared imaging," *J. Appl. Phys.*, vol. 95, no. 7, pp. 3792-3797, April 2004.
- [12] S. D. Holland, C. Uhl, and J. B. Renshaw, "Vibrothermographic crack heating: a function of vibration and crack size," in *Proc. AIP*, 2009, pp. 489-494.
- [13] C. H. Wong, J. C. Chen, and W. Riddell, "Dependence of the sonic IR signal on crack length and crack closure," in *Proc. AIP*, 2009, pp. 481-488.
- [14] X. Han, I. Sarwar, G. Newaz, and L. D. Favro, "Finite element modeling of the heating of cracks during sonic infrared imaging," *J. Appl. Phys.*, vol. 99, no. 7, pp. 074905, April 2006.
- [15] J. Renshaw, S. D. Holland, and R. B. Thompson, "Measurement of crack opening stresses and crack closure stress profiles from heat generation in vibrating cracks," *Appl. Phys. Lett.*, vol. 93, no. 8, pp. 081914, August 2008.

- [16] J. Lu, X. Han, G. Newaz, L. D. Favro, and R. L. Thomas, "Study of the effect of crack closure in sonic infrared imaging," *Nondestruct. Test. Eva.*, vol. 22, no. 2-3, pp. 127-135, August 2007.
- [17] J. Renshaw, S. D. Holland, R. B. Thompson, and C. Uhl, "The effect of crack closure on heat generation on vibrothermography," in *Proc. AIP*, 2009, pp. 473-480.
- [18] X. Han, A. S. Ajanahalli, Z. Ahmed, W. Li, G. M. Newaz, L.D. Favro, and R.L. Thomas, "Finite-element modeling of sonic IR imaging of cracks in aluminum and titanium alloys," in *Proc. AIP*, 2008, pp. 483-490.
- [19] A. Mian, X. Han, S. Islam, and G. Newaz, "Fatigue damage detection in graphite/epoxy composites using sonic infrared imaging technique," *Compos. Sci. Technol.*, vol. 64, no. 5, pp. 657-666, April 2004.
- [20] X. Guo and V. Vavilov, "Crack detection in aluminum parts by using ultrasound-excited infrared thermography," *Infrared Phys. Technol.*, vol. 61, pp. 149-156, November 2013.
- [21] A. S. Rizi, S. Hedayatrasa, X. Maldague, and T. Vukhanh, "FEM modeling of ultrasonic vibrothermography of a damaged plate and qualitative study of heating mechanisms," *Infrared Phys. Technol.*, vol. 61, pp. 101-110, January 2013.
- [22] *Abaqus Documentation 6.14*, Dassault Systems, Johnston, RI, USA, 2005.
- [23] B. Zafosnik, Z. Ren, M. Ulbin, and J. Flasker, "Evaluation of stress intensity factors using finite elements," presented at the 2<sup>nd</sup> FENet Technol. Workshop, Zurich, Switzerland, 2002.
- [24] M. Morbidini and P. Cawley, "A calibration procedure for sonic infrared nondestructive evaluation," *J. Appl. Phys.*, vol. 106, no. 2, pp. 023504, June 2009.
- [25] J. Swevers, F. Al-Bender, C. G. Ganseman, and T. Projogo, "An integrated friction model structure with improved presliding behavior for accurate friction compensation," *IEEE Trans. Automat. Contr.*, vol. 45, no. 4, pp. 675-686, April 2000.



## **Vita**

Vibhor Bhargava was born in 1991, in Jodhpur, India. He received his primary and secondary education in Jaipur, India. He received his B.E. degree in Mechanical Engineering from University of Pune in 2013. From 2013 to 2015, he worked in different roles in multiple companies.

In September 2015, he joined the Mechanical Engineering master's program at the American University of Sharjah as a graduate teaching assistant. During his master's study, he co-authored 1 paper which was presented in ICMSAO'17. His research interests are in computational solid mechanics and nondestructive evaluation of materials.